

THE EVOLUTION OF DUSTY STAR FORMATION AND STELLAR MASS ASSEMBLY IN CLUSTERS: RESULTS FROM THE IRAC 3.6, 4.5, 5.8, AND 8.0 μm CLUSTER LUMINOSITY FUNCTIONS

ADAM MUZZIN,^{1,2,3} GILLIAN WILSON,^{4,5} MARK LACY,⁴ H. K. C. YEE,¹ AND S. A. STANFORD^{6,7}

Received 2007 August 23; accepted 2008 June 27

ABSTRACT

We present a catalog of 99 candidate clusters and groups of galaxies in the redshift range $0.1 < z_{\text{phot}} < 1.3$ discovered in the *Spitzer* FLS. The clusters are selected by their $R_c - 3.6 \mu\text{m}$ galaxy color-magnitude relation using the cluster red-sequence algorithm. Using this cluster sample, we compute the 3.6, 4.5, 5.8, and 8.0 μm cluster LFs. Similar to previous studies, we find that for the bands that trace stellar mass at these redshifts (3.6 and 4.5 μm) the evolution in M^* is consistent with a passively evolving population of galaxies with a high formation redshift ($z_f > 1.5$). Using the 3.6 μm LF as a proxy for stellar luminosity, we remove this component from the MIR (5.8 and 8.0 μm) cluster LFs and measure the LF of dusty star formation/AGNs in clusters. We find that at $z < 0.4$ the bright end of the cluster 8.0 μm LF is well described by a composite population of quiescent galaxies and regular star-forming galaxies with a mix consistent with typical cluster blue fractions; however, at $z > 0.4$, an additional population of dusty starburst galaxies is required to properly model the 8.0 μm LFs. Comparison to field studies at similar redshifts shows a strong differential evolution in the field and cluster 8.0 μm LFs with redshift. At $z \sim 0.65$ 8.0 μm -detected galaxies are more abundant in clusters compared to the field, but thereafter the number of 8.0 μm sources in clusters declines with decreasing redshift, and by $z \sim 0.15$, clusters are underdense relative to the field by a factor of ~ 5 . The rapid differential evolution between the cluster and field LFs is qualitatively consistent with recent field galaxy studies that show that the star formation rates of galaxies in high-density environments are larger than those in low-density environments at higher redshift.

Subject headings: galaxies: clusters: general — galaxies: evolution — galaxies: photometry — galaxies: starburst — Galaxy: fundamental parameters — infrared: galaxies

1. INTRODUCTION

Since the compilation of the first large samples of galaxy clusters almost 50 years ago (Zwicky et al. 1961; Abell 1958), clusters have been used as fundamental probes of the effect of environment on the evolution of galaxies. Over this time, our understanding of this phenomenon has grown significantly, and a basic picture of the formation and evolution of cluster galaxies between $0 < z < 1$ has emerged. Studies of the stellar populations of cluster galaxies via the fundamental plane (e.g., van Dokkum et al. 1998; van Dokkum & Stanford 2003; Holden et al. 2005) and the evolution of the cluster color-magnitude relation (e.g., Ellis et al. 1997; Stanford et al. 1998; Gladders et al. 1998; Blakeslee et al. 2003; Holden et al. 2004; Mei et al. 2006; Homeier et al. 2006; Tran et al. 2007) have shown that the majority of stars in cluster galaxies are formed at high redshift ($z > 2$) and that most of the evolution thereafter is the passive aging of these stellar populations. Studies of the evolution of the near-infrared (NIR) luminosity functions (LFs) of clusters have shown that not only are the stellar populations old, but the bulk of the stellar mass is already

assembled into massive galaxies at high redshift (e.g., De Propris et al. 1999; Toft et al. 2004; Strazzullo et al. 2006; Lin et al. 2006; Muzzin et al. 2007a). Furthermore, it appears that the cluster scaling relations seen locally ($z < 0.1$; e.g., Lin et al. 2003, 2004; Rines et al. 2004), such as the halo occupation distribution, mass-to-light ratio, and galaxy number/luminosity density profile, are already in place by at least $z \sim 0.5$ (e.g., Muzzin et al. 2007b; Lin et al. 2006).

These studies suggest a picture where the formation of the stars in cluster galaxies, as well as the assembly of the galaxies themselves, occurs at a higher redshift than has yet been studied in detail, and that, other than the passive aging of the stellar populations, clusters and cluster galaxies have changed relatively little since $z \sim 1$. This picture appears to be a reasonable zeroth-order description of the evolution of cluster galaxies; however, there are still properties of the cluster population that cannot be explained within this context. In particular, there are significant changes in the morphology (Dressler et al. 1997; Postman et al. 2005; Smith et al. 2005), color (e.g., Butcher & Oemler 1984; Rakos & Schombert 1995; Smail et al. 1998; Ellingson et al. 2001; Margoniner et al. 2001; Loh et al. 2008), and star formation properties (e.g., Balogh et al. 1999; Dressler et al. 1999, 2004; Poggianti et al. 1999, 2006; Tran et al. 2005b; although see Kodama et al. 2004) of cluster galaxies since $z \sim 1$. The fraction of blue, star-forming galaxies increases from almost zero at $z = 0$ to as much as 50% at $z \sim 0.5$ (the so-called Butcher-Oemler effect), and correspondingly, the fraction of S0 galaxies in clusters drops by a factor of 2–3, with similar increase in the number of spiral/irregular galaxies over the same redshift range (Dressler et al. 1997). Naively, these results suggest that gas-rich, star-forming galaxies at high redshift have their star formation truncated by the cluster environment at moderate redshift and become the dominate S0 population

¹ Department of Astronomy and Astrophysics, University of Toronto, Toronto, ON M5S 3H4, Canada.

² Visitor, *Spitzer* Science Center, California Institute of Technology, 220-6, Pasadena, CA, 91125.

³ Current address: Department of Astronomy, Yale University, New Haven, CT 06520-8101; adam.muzzin@yale.edu.

⁴ *Spitzer* Science Center, California Institute of Technology, 220-6, Pasadena, CA 91125.

⁵ Department of Physics and Astronomy, University of California, Riverside, CA 92521.

⁶ University of California, Davis, CA 95616.

⁷ Institute of Geophysics and Planetary Physics, Lawrence Livermore National Laboratory, Livermore, CA 94551.

seen locally. How such a transformation occurs, and how it avoids leaving a notable imprint on the stellar populations, is still not well understood.

Citing an abundance of poststarburst (k+a) galaxies in clusters at $z \sim 0.4$, Poggianti et al. (1999) and Dressler et al. (2004) suggested that there may be an abundance of dusty starburst galaxies in clusters at moderate redshift, and that the dusty starburst and k+a galaxies may represent the intermediate stages between regular star-forming late-type galaxies and S0 galaxies (e.g., Shioya et al. 2004; Bekki & Couch 2003). In particular, they suggested that the cluster e(a)⁸ galaxies would be the best candidates for dusty starburst galaxies because their inferred star formation rates (SFRs) appear larger from H α emission than from [O II] emission. If the cluster environment excites a dusty starburst from harassment, tidal interaction, or ram pressure stripping, then this may quickly deplete a star-forming galaxy of its gas, transforming it first into a k+a galaxy, and then leaving it an S0. More detailed work on two $z \sim 0.5$ clusters by Moran et al. (2005) also showed an abundance of starbursting galaxies conspicuously near the cluster virial radius, suggesting an environmental origin to their “rejuvenation.” *Infrared Space Observatory* (ISO) observations of relatively nearby clusters have detected significant amounts of dust-obscured star formation (e.g., Fadda et al. 2000; Duc et al. 2002; Biviano et al. 2004; Coia et al. 2005), and this has recently been confirmed at even higher redshift ($z = 0.2\text{--}0.8$) by *Spitzer* observations (Geach et al. 2006; Marcillac et al. 2007; Bai et al. 2007; Fadda et al. 2008; Saintonge et al. 2008; Dressler et al. 2008). Despite this, it is currently unclear whether there is a population of dusty starbursts that is sufficiently abundant to be the progenitors of the large number of cluster k+a galaxies.

Alternatively, there is evidence from other cluster samples that the S0 population may simply be the result of the truncation of star formation in infalling late-type galaxies via gas strangulation (e.g., Abraham et al. 1996; Balogh et al. 1999; Treu et al. 2003; Moran et al. 2006) and that no accompanying starburst occurs. Most likely, the star formation and morphology of galaxies are transformed both “actively” (as in a starburst triggered from merging/harassment/tidal forces) and “passively” (from gas strangulation or ram pressure stripping), and the magnitude of each effect varies significantly from cluster to cluster and possibly by epoch, which may explain why studies of small numbers of clusters have found discrepant results. Interestingly, both processes can be active within massive clusters, as was demonstrated by Cortese et al. (2007), who found two interesting galaxies in Abell 1689 and Abell 2667, one of which seems to be undergoing gas strangulation and ram pressure stripping, while the other is experiencing an induced starburst. There is evidence that galaxies in clusters that are less dynamically relaxed have larger SFRs (e.g., Owen et al. 1999; Metevier et al. 2000; Moss & Whittle 2000; Owen et al. 2005; Moran et al. 2005; Coia et al. 2005, and numerous others) and that the accretion of large substructures induces starbursts from harassment and tidal forces.

The most obvious way to understand whether dusty starbursts are important in the evolution of cluster galaxies is to observe their abundances directly in the mid-infrared (MIR). In particular, differences in the MIR LFs of the cluster and field environments can be used to determine if dusty starbursts are more common in the cluster environment. If so, it would suggest that environmental processes may be responsible for triggering these events.

The Infrared Array Camera (IRAC) onboard *Spitzer* provides a unique tool for studying this problem. IRAC images in four bands simultaneously (3.6, 4.5, 5.8, and 8.0 μm), and this is particularly advantageous because 3.6 and 4.5 μm observations are a good proxy for the stellar mass of cluster galaxies between $0 < z < 1$, and 5.8 and 8.0 μm observations are sensitive to emission from warm dust (i.e., from dusty star-forming regions) over the same redshift range. In particular, the polycyclic aromatic hydrocarbons (PAHs) emit strong line emission at rest frame 3.3, 6.2, 7.7, 8.6, and 11.3 μm (e.g., Gillett et al. 1973; Willner et al. 1977). These features, in addition to the warm dust continuum, are sensitive indicators of dusty star formation, and several studies have already shown a good correlation between 8.0 μm flux and SFR⁹ (e.g., Calzetti et al. 2005, 2007; Wu et al. 2005). Therefore, examining the suite of IRAC cluster LFs at redshifts $0 < z < 1$ shows both the evolution of the majority of stellar mass in cluster galaxies and the evolution of dusty star formation in the same galaxies.

The obvious approach to measuring the presence of dusty star formation in clusters is to observe a handful of “canonical” galaxy clusters with IRAC. However, given that determining the LF from a single cluster suffers significantly from Poisson noise and, perhaps most importantly, is not necessarily representative of the average cluster population at a given mass/epoch, a better approach would be to stack large numbers of clusters in order to improve the statistical errors and avoid peculiarities associated with individual clusters. This approach requires targeted observations of numerous clusters, which is time consuming compared to other alternatives. For example, large-area *Spitzer* surveys such as the 50 deg² *Spitzer* Wide-area Infrared Extragalactic Survey¹⁰ (SWIRE; Lonsdale et al. 2003), the 8.5 deg² IRAC Shallow Survey (Eisenhardt et al. 2004), and the 3.8 deg² *Spitzer* First Look Survey¹¹ (FLS; Lacy et al. 2005) are now, or soon to be, publicly available, and these fields already contain significant amounts of optical photometry. These wide optical-IRAC data sets can be employed to find clusters in the survey area itself using optical cluster detection methods such as the cluster red-sequence (CRS) technique (Gladders & Yee 2000, hereafter GY00) or photometric redshifts (e.g., Eisenhardt et al. 2008; Brodwin et al. 2006). Subsequently, the IRAC survey data can be used to study the LFs of clusters at a much larger range of masses and redshifts than could be reasonably followed up by *Spitzer*. Furthermore, these surveys also provide panoramic imaging of clusters out to many virial radii, something that has thus far rarely been attempted because it is time consuming.

Finding clusters with the CRS algorithm is relatively straightforward with the ancillary data available from these surveys. The technique exploits the fact that the cluster population is dominated by early-type galaxies and that these galaxies form a tight red sequence in color-magnitude space. If two filters that span the 4000 Å break are used to construct color-magnitude diagrams, early-type galaxies are always the brightest, reddest galaxies at any redshift (e.g., GY00) and therefore provide significant contrast from the field. The CRS technique is well tested and provides photometric redshifts accurate to $\sim 5\%$ (Gilbank et al. 2007; Blindert et al. 2004), as well as a low false-positive rate ($< 5\%$;

⁸ An e(a) galaxy is defined as a galaxy with $\text{EW}([\text{O II}]) < -5 \text{ \AA}$ and $\text{EW}(\text{H}\delta) > 4 \text{ \AA}$ by Dressler et al. (1999). These are emission-line galaxies with a strong A star component to their spectrum, suggesting a recent, possibly obscured, burst of star formation.

⁹ Although there is a direct correlation between 8 μm flux and SFR, the scatter in the correlation is approximately a factor of 2 for metal-rich galaxies in the local universe, and metal-poor galaxies can deviate by as much as a factor of 50 (e.g., Calzetti et al. 2007). Because of the large scatter and metallicity dependence, throughout this paper we do not use the 8 μm data to quantitatively measure SFRs. Instead, we use the presence of enhanced 8 μm flux as a qualitative indicator of increased dusty star formation.

¹⁰ SWIRE data are publicly available at <http://swire.ipac.caltech.edu/swire/>.

¹¹ The FLS data are publicly available at <http://ssc.spitzer.caltech.edu/fls/>.

e.g., Gilbank et al. 2007; Blindert et al. 2004; Gladders & Yee 2005). The method has been used for the 100 deg² Red-Sequence Cluster Survey (RCS-1; Gladders & Yee 2005) and is also being used for the next-generation, 1000 deg² RCS-2 survey (Yee et al. 2007). Variations of the red-sequence method have also been used to detect clusters in the Sloan Digital Sky Survey (SDSS; the “BCGmax” algorithm; Koester et al. 2007; Bahcall et al. 2003), as well as in the fields of X-ray surveys (e.g., Gilbank et al. 2004; Barkhouse et al. 2006).

In this paper we combine the *Spitzer* FLS R_c band and 3.6 μm photometry and use it to detect clusters with the CRS algorithm. Given the depth of the data and that the $R_c - 3.6 \mu\text{m}$ filter combination spans the rest-frame 4000 Å break to $z > 1$, we are capable of detecting a richness-limited sample of clusters out to $z \sim 1$.

Using the sample of clusters discovered in the FLS, we compute the 3.6, 4.5, 5.8, and 8.0 μm LFs of clusters between $0.1 < z < 1.0$ and study the role of dusty star formation in cluster galaxy evolution. A second paper on the abundance of dusty starburst galaxies detected at 24 μm in the same clusters using the FLS MIPS data is currently underway (A. Muzzin et al. 2008, in preparation).

The structure of this paper is as follows. In § 2 we give a brief overview of the optical, IRAC, and spectroscopic data used in the paper. Section 3 describes the cluster finding algorithm used to detect clusters, and § 4 contains the FLS cluster catalog and a basic description of its properties. In § 5 we present the IRAC cluster LFs, and § 6 contains a discussion of these results, as well as a comparison of the cluster and field LFs. We conclude with a summary in § 7. Throughout this paper we assume an $\Omega_m = 0.3$, $\Omega_\Lambda = 0.7$, $H_0 = 70 \text{ km s}^{-1} \text{ Mpc}^{-1}$ cosmology. All magnitudes are on the Vega system.

2. DATA SET

2.1. *Spitzer* IRAC Data and Photometry

The IRAC imaging data for this project were observed as part of the publicly available, *Spitzer* FLS (for details of the data acquisition and reduction see Lacy et al. 2005). The FLS was the first science survey program undertaken after the telescope’s in-orbit checkout was completed. It covers 3.8 deg² and has imaging in the four IRAC bandpasses (3.6, 4.5, 5.8, and 8.0 μm). The FLS is a shallow survey with a total integration time of only 60 s pixel⁻¹. Because IRAC images all four channels simultaneously, the total integration time is identical in each channel. The resulting 5 σ limiting flux densities are 20, 25, 100, and 100 μJy in the 3.6, 4.5, 5.8, and 8.0 μm bandpasses, respectively. These flux densities correspond to Vega magnitudes of 18.0, 17.2, 15.2, and 14.6 mag, respectively. The 50% completeness limits for the four channels are 18.5, 18.0, 16.0, and 15.4 mag, respectively, and hereafter we use these limits for the cluster finding algorithm (§ 3) and computing the cluster LFs (§ 5). The data were corrected for completeness using a third-order polynomial fit to the survey completeness as a function of magnitude determined by Lacy et al. (2005). Lacy et al. (2005) compared their completeness estimates, made using artificial galaxies, to completeness estimates determined by comparing the recovery of sources in the FLS to a deeper “verification strip.” The completeness was similar using both methods; however, in some cases the latter suggested that it might be higher by $\sim 10\%$ – 15% . When counting galaxies we have multiplied the formal uncertainties by an additional $\pm 20\%$ of the completeness correction to account for this additional uncertainty.

Photometry for the IRAC data was performed using the SExtractor (Bertin & Arnouts 1996) package. For each channel,

four aperture magnitudes plus an isophotal magnitude are computed. The four apertures used are 3, 5, 10, and 20 IRAC pixels in diameter (3.66", 6.10", 12.20", and 24.40"). The aperture magnitudes are corrected for the flux lost outside the aperture due to the large diffraction limit of the telescope and the significant wings of the IRAC point-spread function (PSF). The aperture corrections are computed from bright stars within the FLS field and are listed and discussed further in Lacy et al. (2005). The majority of galaxies with 3.6 $\mu\text{m} > 15.0$ mag are unresolved or only slightly resolved at the resolution of the 3.6 μm bandpass; therefore, the 3 pixel aperture-corrected magnitude provides the best total magnitude. For galaxies that are extended and resolved, this small aperture is an underestimate of their total magnitude. For these galaxies, a “best” total magnitude is measured by estimating an optimum photometric aperture using the isophotal magnitudes. The geometric mean radius of the isophote [$r_m = (A/\pi)^{0.5}$, where A is the isophotal area] is compared to the radius of each of the four apertures used for the aperture magnitudes (r_1, r_2, r_3, r_4). If $r_m < 1.1r_{\text{ap}}$, then that aperture magnitude is chosen as the best total magnitude. For objects with $r_m > 1.1r_4$ the isophotal magnitude is used as the best total magnitude. When measuring the $R_c - 3.6 \mu\text{m}$ colors, we always use the 3 pixel aperture-corrected magnitude, even for resolved galaxies (see discussion in § 2.3).

Object detection was performed separately in all four channels, and these catalogs were later merged using a 1.8" search radius. Tests of this matching (Lacy et al. 2005) show that this radius provides the most reliably matched catalogs.

2.2. Optical Data

The ground-based Cousins R_c band (hereafter “ R band”) imaging used in this study was obtained as part of the FLS campaign and is also publicly available. R -band imaging covering the entire FLS IRAC and MIPS fields was observed on the Kitt Peak 4 m Mayall Telescope using the MOSAIC-1 camera. MOSAIC-1 consists of eight 4096 \times 2048 CCDs and has a field of view of 36' \times 36' with a pixel scale of 0.258" pixel⁻¹. Data reduction was performed using the NOAO IRAF MSCRED package and procedures, and galaxy photometry was performed using the SExtractor (Bertin & Arnouts 1996) package. Typical seeing for the images was $\sim 1.1''$, and the 5 σ limiting magnitude in an aperture of 3" is 24.7 mag. The 50% completeness limit in the same aperture is ~ 24.5 mag. A complete discussion of the data reduction, object finding, and photometry can be found in Fadda et al. (2004). For this study we performed additional photometry to that publicly available in order to measure fluxes in a slightly larger 3.66" aperture, which matches with the smallest aperture of the IRAC data (D. Fadda 2004, private communication).

The mean absolute positional error in the astrometry for the R -band data is 0.35" (Fadda et al. 2004), and the mean positional error in the astrometry of bright (faint) sources in the IRAC catalog is 0.25" (1.0") (Lacy et al. 2005). Given these uncertainties, as well as the large IRAC pixel scale, the R -band catalog was matched to the IRAC catalog by looking for the closest object within 1.5 IRAC pixels (1.8") of each IRAC detection. Tests of matching radii ranging between 0.3 and 3.0 IRAC pixels (0.37"–3.66") showed that the number of matches increased rapidly using progressively larger radii up to ~ 1.5 IRAC pixels and thereafter the gain in the number of matches with increasing radius was relatively modest, suggesting that the majority of additional matches were likely to be chance associations. Given that the IRAC astrometry is calibrated using bright stars from the Two Micron All Sky Survey (2MASS; Skrutskie et al. 2006), whereas the R -band data were astrometrically calibrated using

the USNO-A2.0 catalog (Monet et al. 1998), an additional concern was the possibility of a systematic linear offset between the two astrometric systems. We attempted to iteratively correct for any systematic offset by shifting the IRAC astrometry by the median offset of all matched sources and then rematching the catalogs; however, multiple iterations could not converge to a solution significantly better than the initial $0.2''$ offset seen between the two systems. Given that this offset is less than the quoted positional errors in the two systems, it suggests that any systematic offset between the 2MASS and USNO-A2.0 system in the FLS field is less than the random positional error in the R -band and IRAC data themselves. The iterative refinements increased/decreased the total number of matches by ± 0.05 – 0.3% depending on which iteration. Given these small variations and the lack of further evidence for a systematic offset between the coordinate systems, the final matched catalog uses the original IRAC and R -band astrometry.

In approximately 4% of cases more than one R -band object was located within the search radius. In these cases, the object closest to the IRAC centroid was taken as the match. The space density of R -band sources is approximately 5 times higher than the number of IRAC sources at these respective depths. This suggests that, at most, 20% of R -band sources have an IRAC counterpart at the respective depths.

When there are multiple R -band matches for an IRAC detection, the majority of cases will be where only one of the R -band detections is the counterpart of the IRAC detection, and our approach will provide correct colors. Nevertheless, a certain percentage of the multiple matches will be when two R -band objects, both of which have IRAC counterparts, have these counterparts blended together into a single IRAC detection due to the large IRAC PSF. Because the IRAC source is a blend of two objects, but we use only one R -band counterpart, these objects will be cataloged as brighter and redder than they truly are. However, because only 4% of IRAC sources have multiple R -band matches, and the probability that both of those R -band sources have an IRAC counterpart is roughly $20\%^2 = 4\%$, this suggests that only $4\% \times 4\% = 0.16\%$ of all IRAC sources are blended sources where only one R -band galaxy has been identified as the counterpart.

Although this estimated contamination is small, clusters have greater surface densities of galaxies than the field, and therefore it might be expected that cluster galaxies are blended more frequently than field galaxies. We measured the frequency of multiple matches for galaxies in the fields of the clusters (§ 4) and found that 6.5% of IRAC sources had multiple R -band counterparts, making blending about 1.5 times more common in cluster fields. Even though the rate of blends is higher, it should not have a significant effect on the LFs. Even in the worst case that all 6.5% of IRAC-detected galaxies with multiple R -band matches are blended (not just coincidentally aligned with a faint R -band galaxy in the foreground), and those blends are with a galaxy of comparable luminosity, the values of M^* measured from the LFs would be only ~ 0.05 mag brighter. Given the Schechter function shape of the LF, it is more probable that most galaxies are blended with a fainter galaxy and therefore 0.05 mag is likely to be the upper limit of how significantly blending affects the LFs. This effect is smaller than the statistical errors in the measurement of M^* for the LFs (§ 5); therefore, we make no attempt to correct for it, but note that our M^* values could be systematically high by as much as 0.05 mag.

The large IRAC PSF means that star-galaxy separation using these data is difficult and therefore the classification of each matched object is determined from the R -band data using the CLASS_STAR parameter from SExtractor. This is done using the criteria suggested in Fadda et al. (2004). All objects with $R < 23.5$ with

CLASS_STAR < 0.9 are considered galaxies. For fainter objects with $R > 23.5$, those with CLASS_STAR < 0.85 are considered galaxies. Most stars have $R - 3.6 \mu\text{m}$ colors of ~ 0 in the Vega system. The R -band data are ~ 5 mag deeper than the IRAC data; therefore, most stars detected by IRAC should be robustly removed using this classification.

2.3. Galaxy Colors

The most important ingredient in the cluster red-sequence algorithm is the measurement of accurate colors. Excess noise in the colors causes scatter in the cluster red sequence and reduces the probability that a cluster will be detected. For images with large differences in seeing, PSF shape, and pixel size such as the R band and $3.6 \mu\text{m}$, measuring accurate colors can be problematic. To this end, significant effort was invested in finding the most appropriate way to measure colors with this filter combination.

Studies of the cluster red sequence using telescopes/filters with equivalently large angular resolution differences (e.g., *Hubble Space Telescope* plus ground-based telescopes, Holden et al. 2004; optical and low-resolution IR, Stanford et al. 1998) have typically measured colors by degrading the highest resolution images using the PSF of the lowest resolution images. This is the most accurate way to measure colors and is feasible for a survey of several clusters; however, it is time consuming for a survey the size of the FLS that has more than a million sources detected in the R band. More importantly, because there are so many more galaxies detected in R band than in $3.6 \mu\text{m}$, degrading those images causes numerous unnecessary blends of R -band galaxies, resulting in an increased number of catastrophic color errors. Degrading the resolution also inhibits the potential for detecting distant clusters because the signal-to-noise ratio (S/N) of the faintest R -band objects becomes much worse when they are smeared with a large PSF.

The compromise is to use a fixed aperture that provides accurate colors, yet is as large as possible for the IRAC data (to reduce the need for aperture corrections), and yet is as small as possible to reduce the excess sky noise in the R -band measurement. It is important to use the same diameter apertures for both $3.6 \mu\text{m}$ and R band so that the colors of bright resolved galaxies are measured properly. Galaxies that are small and mostly unresolved require an aperture of only 2–3 times the seeing disk to measure a correct color. In principle, colors for such galaxies can be measured correctly using different-sized apertures for both $3.6 \mu\text{m}$ and R band (i.e., optimized apertures). However, because measuring the color correctly for large galaxies that are resolved in both filters requires that the aperture must be the same size in both filters, we use the same aperture for all galaxies.

After experimenting with apertures ranging in diameter between 1 and 10 IRAC pixels ($1.22''$ – $12.2''$), we determined that the 3 IRAC pixel diameter aperture ($3.66''$) was the optimum aperture because it requires a relatively small aperture correction at $3.6 \mu\text{m}$ ($\sim 10\%$) yet is only slightly larger than three R -band seeing disks, resulting in only a marginal excess sky noise being added to the R -band aperture magnitudes. Using this large fixed aperture means that the photometry of faintest R -band galaxies is not optimized because much of the aperture contains sky. As a result, some potential in discovering the most distant clusters is sacrificed because the faintest red galaxies (i.e., distant red-sequence galaxies) may have excessively large photometric errors. However, most importantly, accurate colors are determined for all galaxies, and overall the approach provides much better photometry than degrading the entire set of survey data.

As an illustration of the quality of colors achievable with this approach, we show the color-magnitude diagram of FLS J171648+5838.6, the richest cluster in the survey, in Figure 1. The typical

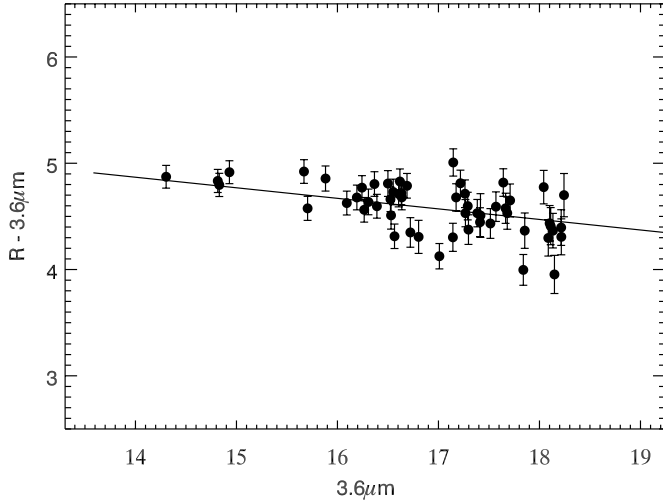


FIG. 1.—Color-magnitude diagram within a 1 Mpc ($2.5'$) diameter of FLS J171648+5838.6 (cluster 44, $z_{\text{spec}} = 0.573$), the richest cluster in the FLS. Several field galaxies with $R - 3.6 \mu\text{m}$ colors > 5.5 have been removed for clarity. The solid line is the best red-sequence model for the cluster (§ 3.1). The intrinsic scatter in the red sequence for this cluster is 0.091 mag for galaxies with $3.6 \mu\text{m} < 17$ mag and 0.151 mag for galaxies with $3.6 \mu\text{m} > 17$ mag and is comparable to the scatter in other clusters at this redshift.

intrinsic scatter of early-type galaxies on the red sequence at the redshift of this cluster ($z_{\text{spec}} = 0.573$) is ~ 0.075 (Stanford et al. 1998; Holden et al. 2004). As a comparison we measure the intrinsic scatter for FLS J171648+5838.6 by subtracting the mean photometric error from the total scatter in quadrature. This is slightly less rigorous than the Monte Carlo methods used by other authors but provides a reasonable estimate of the scatter. For galaxies with $3.6 \mu\text{m} < 17$ mag ($3.6 \mu\text{m} > 17$ mag) the observed scatter of the red sequence is 0.149 (0.225) mag and the mean photometric color error is 0.118 (0.167) mag, resulting in an intrinsic scatter of 0.091 (0.151) mag. We note that without knowing the morphologies of the galaxies we are unable to properly separate early-type galaxies from bluer disk galaxies, and therefore this measurement of the scatter is almost certainly inflated by Sa or Sb galaxies bluer than the red sequence. In particular, these galaxies are generally more prevalent at fainter magnitudes (e.g., Ellingson et al. 2001). However, even without morphological separation, the scatter in the color of red-sequence galaxies is in fair agreement with scatter in the colors of typical red sequences and demonstrates that the $3.66''$ aperture works well for measuring colors.

2.4. Keck, WIYN, and SDSS Spectroscopic Data

A large number of spectroscopic redshifts are available for galaxies in the FLS field from several spectroscopic campaigns. A sample of 642 redshifts were obtained using the HYDRA spectrograph on the Wisconsin-Illinois-Yale-NOAO (WIYN) 3.6 m telescope as part of a program to follow up radio sources in the FLS (Marleau et al. 2007). A set of 1373 redshifts in the FLS field was obtained for galaxies selected by their red $R - K_s$ colors using the Deep Imaging Multi-Object Spectrograph (DEIMOS) on the 10 m KECK II telescope by Choi et al. (2006). Lastly, 1296 redshifts were obtained using the Hectospec Fiber Spectrograph on the 6.5 m MMT by Papovich et al. (2006). The primary targets of that survey were galaxies that are detected in the FLS MIPS 24 μm imaging and have $R < 21.5$ mag. In addition to redshifts from these projects, 1192 redshifts in the FLS field are also available from the SDSS DR5 database (Adelman-McCarthy et al.

2007). In total there are 4503 redshifts at various positions available in the FLS. Of these, 26 are likely to be cluster red-sequence galaxies (see § 3.7).

2.5. Palomar Spectroscopy

In addition to the spectroscopic catalogs available, we also obtained our own long-slit spectroscopy for bright red-sequence galaxies in three clusters with $0.4 < z_{\text{phot}} < 0.6$ in the FLS using the Double Spectrograph (Doublespec) on the 200 inch Hale Telescope at Palomar Mountain (P200). We also obtained multiobject spectroscopy using the COSMIC Spectrograph on the P200 for an additional three clusters with $z_{\text{phot}} < 0.3$. These six clusters were chosen for follow-up because they were among the richest clusters in our preliminary cluster catalogs.

2.5.1. Double-Spectrograph Data

Spectroscopy of bright red-sequence galaxies in clusters FLS J171241+5855.9, FLS J172122+5922.7, and FLS J171648+5838.6 (clusters 16, 38, and 44 listed in Table 1) was performed on 2004 August 17, 18, and 19 with Doublespec on the P200. The observations were made with the “Red” camera using the 316 line mm^{-1} grating blazed at 7150 \AA and a $0.5''$ wide slit, giving a spectral resolution of 2.6 \AA ($\sim 150 \text{ km s}^{-1}$). The Doublespec long slit is $\sim 1.5'$ long, and the angle of the slit on the sky can be rotated. In all three clusters we centered the slit on the brightest cluster galaxy (BCG) and then chose a rotation angle so that we could get at least two other bright objects (preferentially red-sequence galaxies) on the slit.

For FLS J172122+5922.7 and FLS J171648+5838.6 we obtained spectra of three objects in the field, and in FLS J171241+5855.9 we managed four. We obtained three 20 minute exposures for FLS J172122+5922.7 and FLS J171648+5838.6, which have photometric redshifts of 0.57 and 0.55, respectively, and one 20 minute exposure for FLS J171241+5855.9, which has a photometric redshift of 0.39. We also observed a spectroscopic standard, calibration lamps, dome flats, and twilight flats at the beginning of each night. Data reduction and wavelength calibration were performed using the standard IRAF techniques. After one-dimensional spectra were extracted, 7 of the 10 objects had an S/N suitable for cross-correlation. One of the spectra in FLS J171241+5855.9 has a strong emission line at 7056 \AA and no possible identification that puts it near the photo- z of the cluster. This object was therefore considered a field interloper. The remaining six spectra (two per cluster) showed significant absorption features typical of early-type galaxies, and redshifts were obtained by cross-correlating them with an elliptical galaxy spectrum. The redshifts of the galaxies within each cluster were similar ($\Delta z < 0.01$) and are in excellent agreement with the cluster photometric redshift. These spectroscopic redshifts are listed in the cluster catalog (Table 1).

2.5.2. COSMIC Data

Multiobject spectroscopy of both red-sequence galaxies and MIPS 24 μm -detected galaxies in the fields of clusters FLS J171059+5934.2, FLS J171639+5915.2, FLS J171505+5859.6, and FLS J172449+5921.3 (clusters 1, 2, 8, and 10 listed in Table 1) was performed on 2006 May 26, 27, 28, and 29 and 2007 June 15, 16, and 17 using the COSMIC Spectrograph on the 200" Hale Telescope at Palomar Mountain. These observations were made with the 300 line mm^{-1} grating blazed at 5500 \AA with $1''$ wide slits giving a spectral resolution of 8 \AA ($\sim 450 \text{ km s}^{-1}$). These data are part of a larger campaign to study cluster 24 μm sources, and full details of the data reduction, calibration, and cross-correlation will be presented in a future paper (A. Muzzin et al.

TABLE 1
FLS CLUSTER CATALOG

Number (1)	Name (2)	z_{phot} (3)	z_{spec} (4)	R.A. (J2000.0) (5)	Decl. (J2000.0) (6)	$B_{\text{gc},R}$ (Mpc ^{1.8}) (7)	$\epsilon B_{\text{gc},R}$ (Mpc ^{1.8}) (8)	M_{200} ($\times 10^{14} M_{\odot}$) (9)	R_{200} (Mpc) (10)	Centroid (11)
0.....	FLS J172321+5835.0	0.09	0.079 (4)	17 23 21.5	58 35 03.5	237	133	0.51	0.68	BCG
1.....	FLS J171059+5934.2	0.13	0.126 (10)	17 10 59.8	59 34 16.4	521	196	1.82	1.04	BCG
2.....	FLS J171639+5915.2	0.16	0.129 (7)	17 16 39.3	59 15 13.5	326	155	0.85	0.81	BCG
3.....	FLS J172319+6019.5	0.18	0.131 (1)	17 23 19.7	60 19 33.7	358	162	0.99	0.85	BCG
4.....	FLS J171233+5956.4	0.22	...	17 12 33.0	59 56 28.2	534	199	1.89	1.06	RS flux
5.....	FLS J172207+5943.8	0.24	0.271 (2)	17 22 07.9	59 43 52.1	251	132	0.55	0.71	RS flux
6.....	FLS J172618+5934.5	0.27	...	17 26 18.8	59 34 32.3	386	168	1.12	0.89	BCG
7.....	FLS J171618+5907.8	0.27	0.251 (1)	17 16 18.5	59 07 53.0	251	132	0.56	0.71	RS flux
8.....	FLS J171505+5859.6	0.29	0.252 (9)	17 15 05.2	58 59 41.4	310	149	0.78	0.79	BCG
9.....	FLS J171152+6007.7	0.29	0.293 (1)	17 11 52.8	60 07 43.7	381	166	1.09	0.88	RS flux
10.....	FLS J172449+5921.3	0.29	0.253 (9)	17 24 49.0	59 21 22.9	861	252	4.11	1.36	BCG
11.....	FLS J172454+5930.5	0.29	0.273 (1)	17 24 54.4	59 30 32.8	447	181	1.42	0.96	BCG
12.....	FLS J171431+5957.8	0.29	...	17 14 31.1	59 57 52.2	378	165	1.08	0.88	RS flux
13.....	FLS J171455+5836.5	0.30	0.291 (1)	17 14 55.0	58 36 34.7	791	242	3.58	1.30	BCG
14.....	FLS J172505+5932.3	0.34	...	17 25 05.8	59 32 22.9	516	195	1.79	1.04	BCG
15.....	FLS J172008+5949.9	0.36	0.359 (2)	17 20 08.7	59 49 54.1	308	148	0.77	0.79	BCG
16.....	FLS J171241+5855.9	0.38	0.390 (2)	17 12 41.6	58 55 58.7	797	243	3.63	1.31	RS flux
17.....	FLS J171537+5849.4	0.38	0.353 (1)	17 15 37.0	58 49 24.4	590	209	2.23	1.11	RS flux
18.....	FLS J172541+5929.9	0.38	0.366 (1)	17 25 41.7	59 29 59.4	521	196	1.82	1.04	BCG
19.....	FLS J171720+5920.0	0.39	0.395 (1)	17 17 20.3	59 20 05.9	316	150	0.81	0.80	BCG
20.....	FLS J171204+5855.6	0.41	...	17 12 04.7	58 55 36.1	248	131	0.54	0.70	BCG
21.....	FLS J172013+5925.4	0.41	...	17 20 13.1	59 25 29.6	456	183	1.47	0.97	BCG
22.....	FLS J171432+5915.9	0.41	0.394 (1)	17 14 32.6	59 15 54.7	525	197	1.84	1.05	BCG
23.....	FLS J171437+6002.8	0.42	...	17 14 37.8	60 02 53.5	319	151	0.82	0.80	BCG
24.....	FLS J172028+5922.6	0.42	0.281 (1)	17 20 28.9	59 22 38.8	457	183	1.47	0.97	BCG
25.....	FLS J172546+6011.5	0.43	0.450 (1)	17 25 46.3	60 11 30.2	872	253	4.20	1.37	RS flux
26.....	FLS J172026+5916.0	0.43	0.462 (2)	17 20 26.9	59 16 05.0	804	243	3.68	1.31	RS flux
27.....	FLS J171103+5839.9	0.43	...	17 11 03.4	58 39 56.3	528	197	1.86	1.05	RS flux
28.....	FLS J172418+5954.6	0.44	...	17 24 18.5	59 54 37.4	391	169	1.14	0.89	BCG
29.....	FLS J172158+6014.3	0.45	...	17 21 58.3	60 14 20.2	323	152	0.84	0.81	BCG
30.....	FLS J171153+5905.4	0.45	...	17 11 53.6	59 05 28.2	530	198	1.87	1.05	RS flux
31.....	FLS J171447+6018.9	0.48	0.464 (1)	17 14 47.5	60 18 54.7	255	134	0.57	0.71	RS flux
32.....	FLS J172540+5909.5	0.48	...	17 25 40.5	59 09 34.5	600	211	2.29	1.12	RS flux
33.....	FLS J172109+5939.2	0.49	...	17 21 09.1	59 39 15.5	878	254	4.24	1.38	BCG
34.....	FLS J172513+5923.6	0.49	0.518 (1)	17 25 13.1	59 23 36.6	807	244	3.70	1.32	RS flux
35.....	FLS J172142+5921.8	0.52	0.538 (1)	17 21 42.9	59 21 49.1	597	210	2.27	1.12	BCG
36.....	FLS J172342+5941.0	0.52	...	17 23 42.2	59 41 03.5	320	152	0.82	0.80	BCG
37.....	FLS J171622+5915.5	0.53	...	17 16 22.7	59 15 30.7	250	132	0.55	0.70	BCG
38.....	FLS J172122+5922.7	0.53	0.538 (2)	17 21 22.0	59 22 46.3	1287	306	7.89	1.69	BCG
39.....	FLS J172339+5937.2	0.53	...	17 23 39.5	59 37 12.5	318	151	0.82	0.80	BCG
40.....	FLS J171459+6016.7	0.55	...	17 14 59.9	60 16 44.5	730	232	3.15	1.25	BCG
41.....	FLS J171300+5919.4	0.55	...	17 13 00.2	59 19 28.0	591	209	2.23	1.11	RS flux
42.....	FLS J172228+6013.4	0.55	...	17 22 28.8	60 13 24.2	453	182	1.45	0.97	RS flux
43.....	FLS J171405+5900.6	0.55	0.516 (1)	17 14 05.0	59 00 41.7	454	183	1.46	0.97	BCG
44.....	FLS J171648+5838.6	0.56	0.573 (2)	17 16 48.2	58 38 37.7	2040	383	16.6	2.15	BCG
45.....	FLS J172037+5853.4	0.58	...	17 20 37.2	58 53 26.2	518	195	1.80	1.04	RS flux
46.....	FLS J171227+5904.8	0.61	...	17 12 27.6	59 04 53.8	650	219	2.61	1.17	RS flux
47.....	FLS J171452+5917.2	0.61	...	17 14 52.8	59 17 12.9	719	230	3.07	1.24	BCG
48.....	FLS J171104+5858.5	0.61	...	17 11 04.6	58 58 32.7	926	261	4.63	1.42	BCG
49.....	FLS J171634+6009.2	0.62	...	17 16 34.4	60 09 15.2	621	214	2.42	1.14	BCG
50.....	FLS J171420+6005.5	0.63	...	17 14 20.1	60 05 35.3	1131	288	6.40	1.57	BCG
51.....	FLS J171654+6004.8	0.63	...	17 16 54.0	60 04 48.0	510	194	1.76	1.03	RS flux
52.....	FLS J171628+5836.6	0.66	...	17 16 28.5	58 36 40.9	229	124	0.48	0.67	BCG
53.....	FLS J171523+5858.7	0.68	...	17 15 23.9	58 58 47.2	916	260	4.55	1.41	BCG
54.....	FLS J171633+5920.9	0.68	...	17 16 33.9	59 20 54.6	292	143	0.71	0.77	BCG
55.....	FLS J172601+5945.7	0.69	...	17 26 01.1	59 45 47.0	637	217	2.52	1.16	BCG
56.....	FLS J172013+5845.4	0.69	...	17 20 13.0	58 45 26.9	1051	278	5.68	1.51	BCG
57.....	FLS J171836+6006.7	0.70	...	17 18 36.7	60 06 43.3	430	177	1.33	0.94	BCG
58.....	FLS J171903+5851.8	0.70	...	17 19 03.7	58 51 51.1	430	177	1.33	0.94	RS flux
59.....	FLS J172246+5843.7	0.71	...	17 22 46.3	58 43 43.3	429	176	1.33	0.94	BCG
60.....	FLS J171703+5857.9	0.72	...	17 17 03.5	58 57 57.8	912	259	4.51	1.40	BCG
61.....	FLS J172431+5928.3	0.72	...	17 24 31.8	59 28 23.4	220	120	0.44	0.66	BCG
62.....	FLS J171203+6006.6	0.73	...	17 12 03.9	60 06 38.8	289	142	0.70	0.76	RS flux

TABLE 1—*Continued*

Number (1)	Name (2)	z_{phot} (3)	z_{spec} (4)	R.A. (J2000.0) (5)	Decl. (J2000.0) (6)	$B_{\text{gc},R}$ (Mpc ^{1.8}) (7)	$\epsilon_{B_{\text{gc},R}}$ (Mpc ^{1.8}) (8)	M_{200} ($\times 10^{14} M_{\odot}$) (9)	R_{200} (Mpc) (10)	Centroid (11)
63.....	FLS J171430+5901.7	0.73	...	17 14 30.1	59 01 47.1	978	269	5.06	1.46	RS flux
64.....	FLS J171834+5844.6	0.73	...	17 18 34.1	58 44 39.4	359	160	0.99	0.85	BCG
65.....	FLS J172009+6008.0	0.73	0.706 (1)	17 20 09.7	60 08 02.6	426	176	1.31	0.94	BCG
66.....	FLS J172319+5922.2	0.73	...	17 23 19.5	59 22 15.9	356	159	0.98	0.85	BCG
67.....	FLS J172525+5924.7	0.74	...	17 25 25.8	59 24 46.4	633	216	2.49	1.16	RS flux
68.....	FLS J171508+5845.4	0.75	...	17 15 08.8	58 45 27.2	1116	287	6.27	1.56	BCG
69.....	FLS J172148+6016.1	0.77	0.907 (1)	17 21 48.5	60 16 07.7	774	239	3.46	1.29	BCG
70.....	FLS J171454+5958.3	0.77	...	17 14 54.6	59 58 18.4	360	160	1.00	0.86	BCG
71.....	FLS J171511+6028.0	0.77	...	17 15 11.3	60 28 01.4	704	228	2.97	1.22	RS flux
72.....	FLS J172012+5958.3	0.78	...	17 20 12.7	59 58 19.9	705	228	2.97	1.22	RS flux
73.....	FLS J172209+5935.2	0.78	...	17 22 09.4	59 35 16.6	360	160	1.00	0.86	RS flux
74.....	FLS J172035+5928.6	0.78	...	17 20 35.5	59 28 40.4	428	176	1.32	0.94	BCG
75.....	FLS J171411+6027.7	0.78	...	17 14 11.7	60 27 44.3	705	228	2.97	1.22	BCG
76.....	FLS J171545+5853.8	0.78	...	17 15 45.9	58 53 48.6	291	142	0.71	0.76	BCG
77.....	FLS J171556+5859.9	0.79	...	17 15 56.1	58 59 54.3	636	217	2.52	1.16	BCG
78.....	FLS J171932+5929.3	0.79	...	17 19 32.0	59 29 18.5	499	191	1.70	1.02	RS flux
79.....	FLS J172019+5926.6	0.79	...	17 20 19.8	59 26 41.4	291	142	0.71	0.76	RS flux
80.....	FLS J171828+5836.2	0.79	...	17 18 28.7	58 36 13.8	498	191	1.69	1.02	RS flux
81.....	FLS J172304+5832.3	0.81	...	17 23 04.5	58 32 18.6	363	161	1.01	0.86	BCG
82.....	FLS J171657+6004.8	0.82	...	17 16 57.9	60 04 49.3	711	229	3.02	1.23	BCG
83.....	FLS J171945+5909.1	0.84	...	17 19 45.4	59 09 09.1	507	193	1.74	1.03	RS flux
84.....	FLS J171155+6013.1	0.90	...	17 11 55.1	60 13 08.5	522	196	1.82	1.04	RS flux
85.....	FLS J171808+5915.8	0.91	...	17 18 08.7	59 15 50.7	387	168	1.12	0.89	RS flux
86.....	FLS J171223+6015.1	0.95	...	17 12 23.7	60 15 09.4	605	211	2.32	1.13	RS flux
87.....	FLS J171051+5930.8	1.02	...	17 10 51.8	59 30 50.5	760	237	3.36	1.27	BCG
88.....	FLS J172147+6011.5	1.02	...	17 21 47.3	60 11 35.7	277	141	0.65	0.74	BCG
89.....	FLS J171852+6009.9	1.02	...	17 18 52.7	60 09 56.9	485	189	1.62	1.00	RS flux
90.....	FLS J171221+6010.6	1.03	...	17 12 21.2	60 10 41.0	349	160	0.95	0.84	BCG
91.....	FLS J171431+5946.9	1.06	...	17 14 31.9	59 46 59.5	425	177	1.31	0.94	RS flux
92.....	FLS J171117+5902.8	1.06	...	17 11 17.5	59 02 48.6	287	144	0.69	0.76	BCG
93.....	FLS J172126+5856.6	1.11	1.045 (4)	17 21 26.4	58 56 41.7	646	218	2.58	1.17	BCG
94.....	FLS J171227+6015.2	1.14	...	17 12 27.0	60 15 16.7	448	182	1.43	0.96	BCG
95.....	FLS J172045+5834.8	1.17	...	17 20 45.3	58 34 50.9	386	169	1.12	0.89	RS flux
96.....	FLS J172113+5901.0	1.24	...	17 21 13.8	59 01 05.7	338	158	0.90	0.83	RS flux
97.....	FLS J171223+6006.9	1.27	...	17 12 23.6	60 06 56.4	208	124	0.41	0.64	RS flux
98.....	FLS J171942+5938.3	1.38	...	17 19 42.8	59 38 23.2	374	165	1.06	0.87	RS flux

NOTES.—Col. (1): Number. Col. (2): Name. Col. (3): Photometric redshift estimated from red sequence color. Col. (4): Mean spectroscopic redshift of galaxies with red sequence weights >0.2 ; the number of spectroscopic redshifts is included in parentheses. Cols. (5) and (6): Right ascension and declination. Units of right ascension are hours, minutes, and seconds, and units of declination are degrees, arcminutes, and arcseconds. Col. (7): Cluster richness parameterized by $B_{\text{gc},R}$. Col. (8): Error in $B_{\text{gc},R}$. Col. (9): M_{200} estimated from $B_{\text{gc},R}$ using eq. (1). Col. (10): R_{200} estimated from $B_{\text{gc},R}$ using eq. (2). Col. (11): Best centroid of the cluster.

2008, in preparation). We obtained 17, 16, 12, and 20 good-quality spectra in the fields of FLS J171059+5934.2, FLS J171639+5915.2, FLS J171505+5859.6, and FLS J172449+5921.3, respectively, and redshifts were determined using cross-correlation. Including the data from the other spectroscopic campaigns, the field of FLS J171059+5934.2 has 10 galaxies with $\bar{z} = 0.126$, the field of FLS J171639+5915.2 has seven galaxies with $\bar{z} = 0.129$, the field of FLS J171505+5859.6 has nine galaxies with $\bar{z} = 0.252$, and the field of FLS J172449+5921.3 has 12 galaxies with $\bar{z} = 0.253$. These redshifts are included in the cluster catalog (Table 1).

2.6. Keck DEIMOS Spectroscopy of FLS J172126+5856.6

Spectroscopy was obtained of the candidate cluster FLS J172126+5856.6 (cluster 93 in Table 1) with DEIMOS (Faber et al. 2003) on the 10 m Keck II telescope. On the night of 2005 September 1, we obtained three 1800 s exposures on the same mask in nonphotometric conditions with $\sim 1.3''$ seeing. The 600ZD grating ($\lambda_{\text{blaze}} = 7500 \text{ \AA}$; $\Delta\lambda_{\text{FWHM}} = 3.7 \text{ \AA}$) and a GG455 order-blocking filter were used. The DEIMOS data were processed using a slightly

modified version of the pipeline developed by the DEEP2 team at UC-Berkeley.¹² Relative flux calibration was achieved from observations of standard stars from Massey & Gronwall (1990).

Slits were preferentially placed on candidate red-sequence galaxies, allowing a total of 10 slits on likely cluster members. Of the 10 candidate red-sequence galaxies, 5 had sufficient S/N for determining redshifts, and 4 had redshifts $\Delta z < 0.01$ from each other, with the $\bar{z} = 1.045$. These redshifts are included in the cluster catalog (Table 1).

3. CLUSTER FINDING ALGORITHM

The cluster finding algorithm employed in this study is essentially the CRS algorithm of GY00 and Gladders & Yee (2005) with some minor modifications. Here we outline only the major steps and refer to those papers for a more detailed explanation of the procedures.

The CRS algorithm is motivated by the observation that early-type galaxies dominate the bright end of the cluster LF and that

¹² See <http://astro.berkeley.edu/~cooper/deep/spec2d/>.

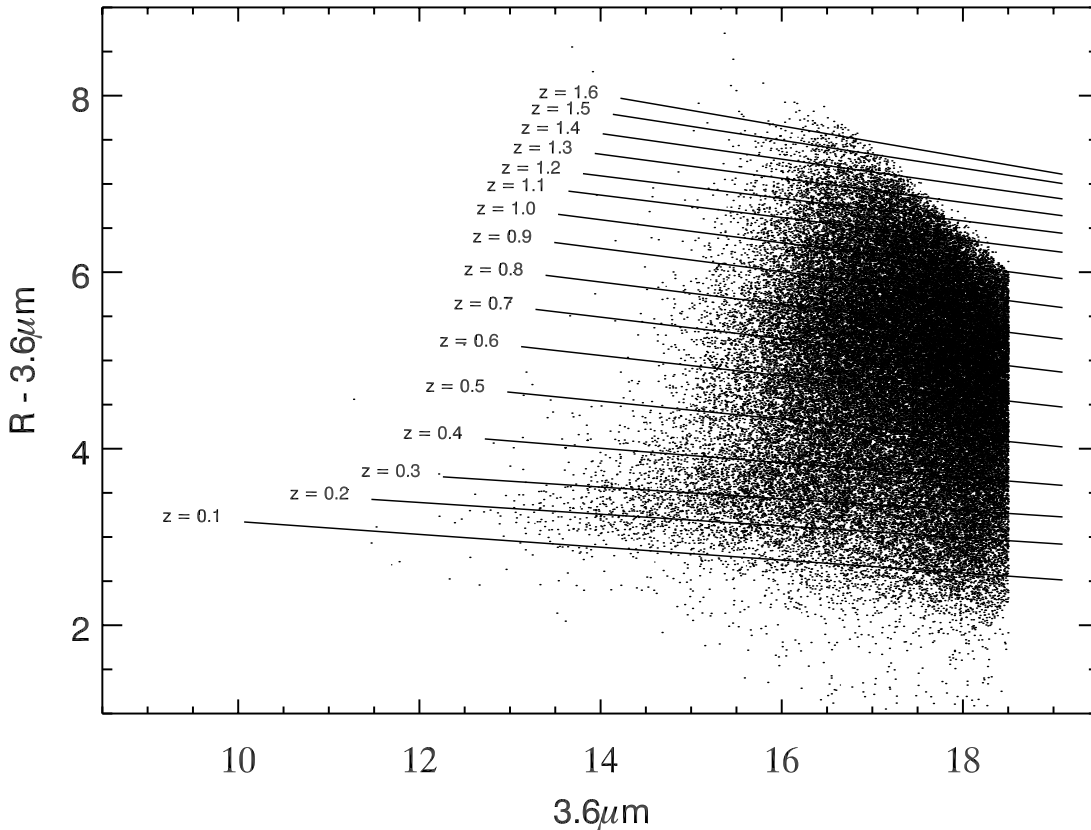


FIG. 2.—Observed color-magnitude diagram for all galaxies in the FLS. The solid lines are fiducial red-sequence models at different redshifts generated using the Bruzual & Charlot code. The redshift of each model is labeled in the figure. The bulk of the shift in color with redshift of the models is due to bandpass shifting or “ k -correction,” not because of evolution in the rest-frame colors of the galaxies.

these galaxies always follow a tight red sequence in the color-magnitude plane. At increasing redshift the observed red-sequence color becomes redder,¹³ and because this change in color follows closely the predictions from a passively evolving stellar population, the color can be used as a robust photometric redshift estimate for a cluster. In order to apply the CRS algorithm, slices are made in the color-magnitude plane of a survey. Galaxies are then assigned weights based on the probability that they belong to a particular slice. This probability is determined by the color and the photometric error in the color. Once color weights for each galaxy in each slice have been assigned, each galaxy is also assigned a magnitude weight. Magnitude weighting is done because bright red-sequence galaxies are more likely to be members of clusters than faint ones.

Once each galaxy is assigned a color and magnitude weight for each slice, the positions of each galaxy are plotted for each slice with their respective weights. The resulting “probability map” for each slice is then smoothed and peaks in these maps represent likely cluster candidates. In the following subsections we discuss in more detail the steps in our version of the algorithm.

3.1. Red-Sequence Models

The first step in finding clusters with the CRS is to model the color, slope, and intercept of the cluster red sequence as a func-

tion of redshift. This was done by making simulated single-burst galaxies using all available metallicities from the Bruzual & Charlot (2003) spectral synthesis code. The models are constructed with 50% of the stars forming in a single burst at $t = 0$ and the remainder forming with an exponentially declining SFR of $\tau = 0.1$ Gyr. Using a range of metallicities causes the color of each galaxy to be slightly different at $z = 0$, with the most metal-rich galaxies being the reddest. The absolute magnitude of each galaxy with a different metallicity is normalized using the $U - V$, $V - I$, and $J - K$ red sequences of Coma (Bower et al. 1992) assuming that a metallicity gradient with magnitude is the primary source of the slope of the red sequence. Normalizing the absolute magnitude of each galaxy this way allows us to reproduce models with the correct red-sequence color and slope with redshift.

There is increasing evidence that the slope of the red sequence is not only caused by a metallicity sequence but is also the product of an age sequence, with the less luminous galaxies being both more metal-poor and younger (e.g., Nelan et al. 2005; Gallazzi et al. 2006). Examination of spectroscopically confirmed clusters in the FLS shows that the pure metallicity sequence used in our models reproduces the red-sequence slope and color quite well, and because we are only interested in a fiducial red-sequence model for detecting clusters and determining photometric redshifts, no further tuning of the ages of galaxies along the sequence is done.

Once the absolute magnitude of each model galaxy is normalized using the Coma red sequences, linear fits to the $R - 3.6 \mu\text{m}$ versus $3.6 \mu\text{m}$ color-magnitude relations of the model galaxies between $0.1 < z < 1.6$ are made. A high density of redshift models is fitted so that there is significant overlap in color space (185 slices between $0.1 < z < 1.6$). This assures that no clusters are missed because they have colors between the finite number

¹³ The observed-frame color of the red sequence becomes redder with increasing redshift because of band shifting. The rest-frame color change due to passive evolution actually makes galaxies bluer at higher redshift but is a small effect for a single-burst population formed at high redshift. Because the change in observed-frame color is dominated by the k -correction from an old stellar population, it increases monotonically with redshift and provides a good estimate of the cluster redshift.

of models, and it also allows for increased precision in the photometric redshifts.

We computed two sets of single-burst models, one with a formation redshift $z_f = 2.8$ and another with $z_f = 5.0$. These two sets of models produce nearly identical observed red sequences at $z < 1.1$ but begin to diverge at higher redshifts. There is evidence from previous studies of the fundamental plane (e.g., van Dokkum et al. 1998; van Dokkum & Stanford 2003, and many others), evolution of the color-magnitude diagram (Stanford et al. 1998; Holden et al. 2004), and K -band LF (De Propris et al. 1999; Lin et al. 2006; Muzzin et al. 2007a) that a $z_f \sim 3$ model is appropriate for cluster early-type galaxies; however, the uncertainties in these studies are fairly large. There is also evidence that many of the most massive field early-type galaxies formed the majority of their stars at $z > 5$ (McCarthy et al. 2004; Glazebrook et al. 2004), so the possibility remains that a $z_f = 5.0$ is more appropriate. Regardless, the majority of the systems we have discovered are at $z < 1.1$; therefore, the z_f uncertainty does not affect the photometric redshifts of these systems. For systems at $z > 1.1$, the redshift can be considered an upper limit. For example, the photo- z for a cluster at $z = 1.3$ in the $z_f = 2.8$ model would be $z \sim 1.2$ in the $z_f = 5.0$ model.

To illustrate the depth of the survey and the location of the red-sequence models, Figure 2 shows the $R - 3.6 \mu\text{m}$ versus $3.6 \mu\text{m}$ color-magnitude diagram for all galaxies in the FLS with some of the $z_f = 2.8$ red-sequence models overlaid. The density of galaxies with $M \sim M^*$ begins to drop off significantly for the $z > 1.2$ red-sequence models because of the depth of the R -band data [$M^*(3.6 \mu\text{m}) \sim 17.0$ mag at $z = 1.2$]; therefore, we consider $z \sim 1.2$ the upper limit at which we can reliably detect clusters. Remarkably, the red-sequence models are even well separated in color space at $z < 0.5$, where the $R - 3.6 \mu\text{m}$ filters do not span the 4000 Å break. This is caused by the large wavelength separation between the bands and the wide $3.6 \mu\text{m}$ filter, which has a strongly redshift-dependent negative k -correction. Although the k -correction in R band evolves slowly with redshift out to $z \sim 0.5$, the k -correction for $3.6 \mu\text{m}$ is significant and therefore the $R - 3.6 \mu\text{m}$ color is still a sensitive redshift indicator.

3.2. Color Weights

Once red-sequence models have been made, weights based on the probability that a galaxy belongs within a color slice are computed. The typical 1σ scatter in the local cluster color-magnitude relation is ~ 0.075 mag (e.g., Lopez-Cruz et al. 2004; Bower et al. 1992). The scatter has been measured in clusters to $z \sim 1$, where it remains remarkably consistent (e.g., Stanford et al. 1998; Gladders et al. 1998; Blakeslee et al. 2003). Thereafter, it may become somewhat more scattered (Holden et al. 2004). Assuming that this relation holds to $z \sim 1.3$, color weights (with values ranging from 0 to 1) are assigned by computing the overlapping area of a galaxy's color with the red sequence assuming a red-sequence intrinsic dispersion of 0.075 mag and assuming that the galaxy's color is represented by a Gaussian centered on the measured color with a 1σ dispersion equal to the color error (see, e.g., GY00, Fig. 3). Using this method, the weight of a bright galaxy lying directly on the red sequence with a color error significantly narrower than the width of the red sequence is 1.0. The same galaxy with a color error equal to the dispersion in the red sequence has a weight of 0.67. Color weights are computed for all galaxies in all 185 color slices.

3.3. Magnitude Weights

In addition to the color weights, galaxies are also weighted based on their magnitude relative to a fiducial M^* value. Cluster

early-type galaxies are usually the brightest, reddest galaxies at a given redshift; therefore, the brightest galaxies within a color slice are more likely to be cluster galaxies and should be given extra weight. The distribution of magnitude weights was defined as $P(M)$ by GY00 (see their § 4.3). We compute the $P(M)$ using the data themselves, as suggested by those authors, and when doing so we consider objects within the 1st percentile highest density regime as “cluster” galaxies. This is a slightly more strict cut than the 10th percentile cut used by GY00; however, the fact that IR-selected galaxies are more strongly clustered than optically selected galaxies justifies using a more stringent cut.

3.4. Probability Maps

Once the magnitude and color weights for all galaxies in each of the individual color slices have been computed, a probability map of each slice is created. The map is a spatial galaxy density map of the survey within each redshift slice. The map is made using pixels that are 125 kpc in physical size at the redshift of each slice. The probability flux from each pixel is determined by placing each galaxy on the pixel that corresponds to its location in the survey, weighted by the product of its color and magnitude weights. Once each slice is constructed this way, it is smoothed with the exponential kernel suggested in GY00 (their eq. [3]).

3.5. Noise Maps

The noise properties of the probability maps of different color/redshift slices are usually different. In particular, the maps of the highest redshift slices tend to have large noise peaks because the survey is only as deep as $\sim M^*$ in those slices.

The lower redshift probability maps have a smoother background because there are numerous $M > M^*$ galaxies that are more evenly distributed spatially and have a low probability of belonging to any slice because they have a large color error. The higher redshift maps are shallower, thereby lacking the $M > M^*$ galaxies that provide this smooth background.

If peak finding is run on all probability maps using similar detection parameters, it produces significantly different numbers of detections in different slices. In particular, almost any noise in the highest redshift maps results in the detection of a “cluster.”

To circumvent this problem, the parameters of the peak finding for each map can be tuned individually in order to produce a reasonable number of detections in each slice; however, the resulting cluster catalog is clearly biased by what is considered a “real” detection in a given map. It is preferable to have a cluster catalog that is as homogeneously selected as possible and based on a quantitative selection. Therefore, “noise” maps are constructed and are added to each probability map to homogenize their noise properties.

The noise maps are constructed by adding fake red-sequence galaxies to each pixel of the probability maps. Adding a constant background of fake galaxies does not change the noise properties of a map because it is the variance in the number of background galaxies that determines the noise. We experimented with a variety of variances to add but settled that the variance from the photometric color errors of six M^* red-sequence galaxies per pixel provided the best results. This level of noise removes the spurious detections in the highest redshift slices but does not add so much noise as to wash out the majority of the poorer clusters in the lower redshift slices.

The noise in each pixel is calculated by first determining the average color error of an M^* red-sequence galaxy using the survey data. Once the average color error per slice is tabulated, the weights of six M^* red-sequence galaxies are Monte Carlo simulated for each pixel of a noise map assuming that the colors are

normally distributed around the red sequence with a dispersion equal to the mean color error. These simulated weights are then assigned to each pixel of the noise map and each noise map is added to the appropriate cluster probability map. This approach thereby implicitly defines a “cluster” as an overdensity detectable above the Poisson noise from six M^* background red-sequence galaxies at any redshift. The noise+clusters maps have similar noise properties for every slice, and peak finding can be run using identical parameters for all maps.

We note that in our simple empirical method for homogenizing the noise in the probability maps the added noise is Poissonian, not clustered like the underlying background galaxy distribution. Despite this, the noise maps technique works extremely well, effectively smoothing out spurious noise spikes in the highest redshift probability maps. In principle, a more sophisticated method that includes the clustering properties of background galaxies could be implemented; however, for our purposes such an approach is unnecessary. Only the detection probability of poorest clusters near the significance limit is affected by different choices in noise maps. Galaxies from the poorest clusters do not contribute significantly to the LFs, which are dominated by counts from more massive systems, and therefore we do not consider this issue further.

3.6. Cluster Detection

Once the combined noise probability maps have been made, peaks are detected in each map using SExtractor. The peak finding is done differently from GY00 in that the individual two-dimensional slices are searched instead of merging the slices into a three-dimensional data cube and searching for three-dimensional peaks. It is unclear how these two methods compare; however, they are likely to be similar and searching the slices individually permits easy visual inspection of the sources on each map, which allows us to check any problems that have occurred with peak finding or in the generation of the map. Pixels 5σ above the background are flagged, and 25 connected pixels are required to make a detection.

The slices are close in color space and therefore clusters (particularly rich ones) are detected in more than one color slice. The same cluster is identified in multiple color slices by merging the slice catalogs using a matching radius of 8 pixels (1 Mpc). Clusters found across as many as 20 color slices are connected as being the same object. The color slices are not linear in redshift, but 20 slices correspond to $\Delta z \sim \pm 0.06$. These combined spatial and color limits for connecting clusters imply that clusters with separations >1 Mpc in transverse distance and >0.06 in redshift space can be resolved into distinct systems.¹⁴ This level of sensitivity is similar to that found by Gladders & Yee (2005) using $R - z'$ colors to select clusters. They also demonstrated that subclumps at redshift spacings much less than this are likely to be associated subclumps or infalling structures related to the main body of the cluster.

3.7. Photometric Redshifts

Each cluster is assigned the photometric redshift of the color slice in which it is most strongly detected. The strength of the detection is determined by using SExtractor to perform aperture photometry of each cluster on each probability map. This provides a “probability flux,” and the cluster is assigned to the slice in which it has the largest probability flux.

¹⁴ The color slices are closer together at $z > 1$, and only systems with $\Delta z > 0.12$ can be resolved at this redshift. We note that although the overall level of projections is likely to be low, because of the bunching up of the color slices, the highest redshift clusters will be the most susceptible to projection effects.

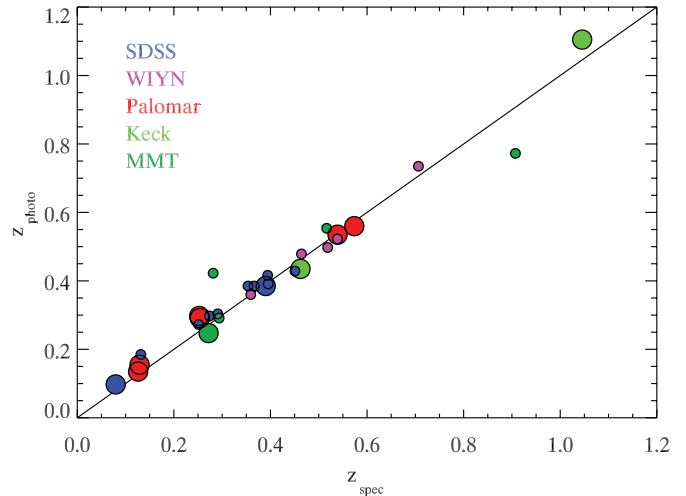


FIG. 3.—Photometric vs. spectroscopic redshift for clusters in the FLS field. The color of the circle corresponds to the telescope/project where the spectroscopic redshifts were obtained (see § 2). Large circles denote clusters with more than one spectroscopic redshift, while small circles denote clusters with only one spectroscopic redshift. Excluding the one large outlier at $z_{\text{spec}} \sim 0.9$, the rms scatter is $\Delta z = 0.04$.

The large number of spectroscopic redshifts available for the FLS can be used to verify the accuracy of the red-sequence photometric redshifts. Examining the spectroscopic catalog for galaxies within a 1 Mpc circle around each cluster shows that there are numerous galaxies with spectroscopic redshifts in the field of many of the clusters. The spectroscopic targets were chosen with a variety of selection criteria (none of which preferentially select early-type galaxies); therefore, the majority of galaxies with redshifts are foreground or background galaxies. We use only the spectroscopic redshifts for galaxies that have a combined magnitude and color weight of >0.2 in order to preferentially select likely cluster members. This cut in weight is used because it corresponds to the typical combined magnitude and color weight of $M < M^*$ red-sequence galaxies. Once the cut is made, there are 23 clusters that have at least one spectroscopic redshift for a likely cluster red-sequence galaxy. Remarkably, there are 26 galaxies that meet this criterion, and 24 of these have a spectroscopic redshift <0.1 from the photometric redshift of the cluster. This illustrates the effectiveness of the red-sequence color at estimating photometric redshifts provided that the galaxy has a high probability of being a cluster early type.

In Figure 3 we plot spectroscopic versus photometric redshift for these 23 clusters plus the additional six for which we obtained our own spectroscopic redshifts (§ 2.5). The straight line marks a one-to-one correlation. Large circles represent clusters with more than one galaxy with a redshift consistent with being in the cluster. Small circles represent clusters with a single spectroscopic redshift. Excluding the large single outlier with $z_{\text{spec}} \sim 0.9$ (which is likely to be a bluer galaxy at high redshift based on its spectrum and IRAC colors; see § 6.3), the rms scatter in the cluster spectroscopic versus photometric redshift is $\Delta z = 0.04$, demonstrating that the photometric redshifts from the red-sequence algorithm work extremely well.

The accuracy of the photometric redshifts from the FLS sample is comparable to the accuracy of the RCS surveys (Yee et al. 2007; Gladders & Yee 2005), which use $R - z'$ color selection, even though the $R - 3.6\ \mu\text{m}$ colors have larger photometric errors than the $R - z'$ colors. It is likely that this is because the model red-sequence colors change much more rapidly with redshift in $R - 3.6\ \mu\text{m}$ than in $R - z'$ ($R - 3.6\ \mu\text{m}$ spans 2 mag between

$z = 0.5$ and 1.0 , whereas it spans only 1 mag in $R - z'$). The larger change in the $R - 3.6 \mu\text{m}$ colors with redshift means that photometric measurement errors should correspond to smaller errors in photometric redshift.

3.8. B_{gc} Richness Parameter

The final step in the selection of the cluster sample is to cut low-richness detections from the catalog. The false-positive rate is higher for low-richness systems (i.e., galaxy groups), and we prefer to restrict our analysis of the cluster LFs to a high-confidence sample of massive clusters. The cluster richnesses are measured quantitatively using the B_{gc} richness parameter (Longair & Seldner 1979; for a detailed look at the application of B_{gc} to measuring cluster richnesses see Yee & Lopez-Cruz 1999). B_{gc} is the amplitude of the three-dimensional correlation function between cluster galaxies and the cluster center. B_{gc} is measured within a fixed aperture (typically 500 kpc radius) and is well correlated with cluster physical parameters such as velocity dispersion (σ), X-ray temperature (T_X), and the radius at which the mean density of the cluster exceeds the critical density by a factor of 200 (R_{200} ; e.g., Yee & Lopez-Cruz 1999; Yee & Ellingson 2003; Gilbank et al. 2004; Muzzin et al. 2007b).

Gladders & Yee (2005) introduced a new form of the B_{gc} parameter, counting the overdensity of red-sequence galaxies within a fixed aperture, rather than all galaxies, and defined this new parameter as $B_{\text{gc},R}$. This form of richness suffers less from cosmic variance in the background because red-sequence galaxies provide better contrast with the field, and therefore it is a more robust estimate of the cluster richness. We use $B_{\text{gc},R}$ rather than B_{gc} for determining the richnesses of the FLS clusters. The net number of $3.6 \mu\text{m}$ red-sequence galaxies with $M < M^* + 1.0$ (where M^* is determined from the data themselves; see § 5.1) are counted within a fixed aperture of 500 kpc radius. The model red sequences from § 3.1 are used, and galaxies within ± 0.3 in color are considered to belong to the red sequence.

Systems with $B_{\text{gc},R} < 200$ are removed from the cluster catalog. The $B_{\text{gc}}-M_{200}$ relation of Yee & Ellingson (2003) implies that this corresponds to removing groups with $M_{200} < 6.6 \times 10^{13} M_{\odot}$, where M_{200} is defined as the mass contained within R_{200} . Groups with masses below this typically have only $\sim 5-10$ bright galaxies (e.g., Balogh et al. 2007), making them difficult to select robustly with the CRS algorithm. The systems that are removed by the richness cut are typically tight compact groups of three to four extremely bright galaxies that are the same color. Although they are not rich, they have a strong probability of being detected by the CRS algorithm because of their luminosity and compactness. It is likely that the majority of these systems are bona fide low-richness galaxy groups; however, we have no way of verifying the false-positive rate for these systems.

Before these low-richness systems are cut from the catalog, there are 134 cluster candidates between $0.1 < z < 1.4$ in the FLS field. Removing systems with $B_{\text{gc},R} < 200$ leaves a total of 99 candidate clusters in the sample.

3.9. Cluster Centroids

Defining a centroid for clusters can be a challenging task, yet it is extremely important because properties determined within some aperture around the cluster (such as richness, or LF) can vary strongly with the choice of centroid. In many cluster studies the location of the BCG is used as the center of the cluster. This is a reasonable definition as frequently the BCG lies at the center of the dark matter halo and X-ray emission; however, there are also many examples where it does not. Furthermore, not all clusters have an obvious BCG, particularly at higher redshift.

Given these issues, two centroids are computed for the FLS clusters, one based on the location of the peak of the red sequence probability flux in the probability maps, and the other based on the location of the BCG within 500 kpc of this centroid. In order to avoid bright foreground galaxies, the brightest galaxy in the field with a red-sequence weight > 0.4 is designated as the BCG. Eye examination of the clusters shows that this criterion is effective at choosing what appears visually to be the correct galaxy; however, because it chooses only a single galaxy, this technique is still potentially susceptible to red low-redshift field interlopers.

When computing the cluster LFs, only one of the centroids can be used. We define an “optimum” centroid for each cluster using the $B_{\text{gc},R}$ parameter. $B_{\text{gc},R}$ is computed at both centroids, and the optimum centroid is the centroid that produces the maximum value of $B_{\text{gc},R}$. This approach is simplistic, but because B_{gc} is the correlation amplitude between the cluster center and galaxies, the centroid that produces the largest value should be the best centroid of the galaxy population.

4. PROPERTIES OF THE CLUSTER CATALOG

The final cluster catalog of 99 clusters and groups is presented in Table 1. Where spectroscopic redshifts are available for high-probability cluster members they are listed in column (3), with the number of redshifts in parentheses. For each cluster we also compute an estimate of R_{200} and M_{200} . The M_{200} values are estimated using the correlation between B_{gc} and M_{200} measured by Muzzin et al. (2007b) for 15 X-ray-selected clusters at $z \sim 0.3$ in the K band. The K -band and $3.6 \mu\text{m}$ bandpasses sample similar parts of a galaxy’s spectrum at $0.1 < z < 1.5$; therefore, it is reasonable to assume that B_{gc} values measured in both these bands will be comparable. The best-fit relation between M_{200} and B_{gc} is

$$\log M_{200} = (1.62 \pm 0.24) \log B_{\text{gc}} + (9.86 \pm 0.77). \quad (1)$$

Muzzin et al. (2007b) did not measure the correlation between B_{gc} and R_{200} in the K band, although Yee & Ellingson (2003) showed a tight correlation for the same clusters using r -band-selected B_{gc} . Using the Muzzin et al. (2007b) K -band data, we fit the correlation between these parameters for those clusters and find that the best-fit relation is

$$\log R_{200} = (0.53 \pm 0.09) \log B_{\text{gc}} - (1.42 \pm 0.29). \quad (2)$$

The rms scatter in the $M_{200}-B_{\text{gc}}$ relation is 35%, and for the $R_{200}-B_{\text{gc}}$ relation it is 12%. These scatters are similar to that measured between M_{200} and K -band-selected richness (parameterized by N_{200}) at $z \sim 0$ by Lin et al. (2004). The values of M_{200} and R_{200} derived from these equations are listed in columns (9) and (10) of Table 1, respectively.

We caution that these equations have only been calibrated using rich clusters, and that extrapolating to lower richness clusters such as those in the FLS may not be appropriate. The lowest richness cluster in the Muzzin et al. (2007b) sample has a richness of $\log B_{\text{gc}} = 2.8$, yet the majority of clusters in the FLS (70/99) have lower richnesses than this. There is evidence from both observations (e.g., Lin et al. 2004) and numerical simulations (e.g., Kravtsov et al. 2004) that the same power-law correlation between cluster galaxy counts (which are closely related to B_{gc}) and M_{200} extends to richnesses well lower than our $B_{\text{gc},R} > 200$ cut, and therefore it probably is not too unreasonable to extrapolate equations (1) and (2) to lower richnesses.

Using an indirect method to estimate M_{200} and R_{200} means that reliable errors in R_{200} and M_{200} cannot be computed for individual clusters; however, the rms scatters in the correlations are

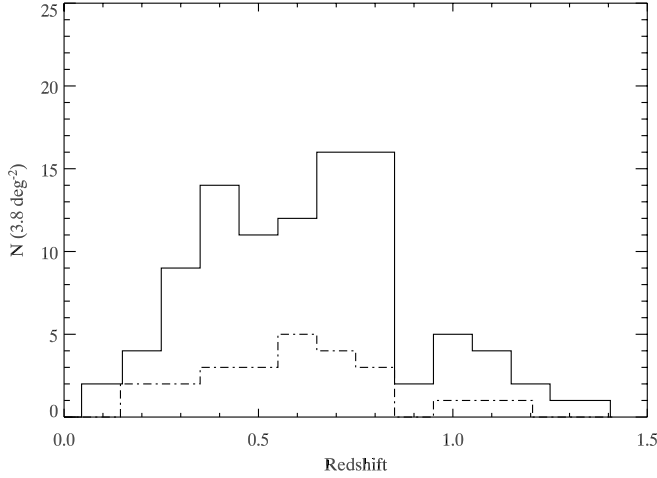


FIG. 4.— Redshift distribution of clusters in the FLS. The solid histogram is for all clusters, and the dot-dashed histogram is for clusters with $M_{200} > 3 \times 10^{14} M_{\odot}$.

at least indicative of the average uncertainty in the measurement of the parameters for the sample. Therefore, we suggest that the average errors in the M_{200} and R_{200} values listed in Table 1 are $\pm 35\%$ and 12% , respectively, but that the error in a particular cluster can be several times larger or smaller.

In Figure 4 we plot a histogram of the number of clusters as a function of redshift in the FLS. The solid histogram shows the distribution of all clusters, and the dot-dashed histogram shows the distribution of clusters with $M_{200} > 3 \times 10^{14} M_{\odot}$ ($B_{gc,R} > 700$). Similar to the predictions of numerical simulations (e.g., Haiman et al. 2001), the number of clusters peaks at $z \sim 0.6$. Qualitatively, the distribution of clusters is also similar to that found by Gladders & Yee (2005) in comparable size patches; however, the cosmic variance in the number of clusters in $\sim 4 \text{ deg}^2$ patches is too large to make a meaningful comparison between the selection of clusters in the $R - z'$ bandpasses and the $R - 3.6 \mu\text{m}$ bandpasses.

We plot the locations of the clusters superposed on the $3.6 \mu\text{m}$ image of the FLS field in Figure 5 as open circles. Large and small circles represent clusters with $M_{200} > 3 \times 10^{14} M_{\odot}$ and $M_{200} < 3 \times 10^{14} M_{\odot}$, respectively, and clusters with photometric redshifts $0.1 < z < 0.4$, $0.4 < z < 0.8$, and $z > 0.8$ are plotted as blue,

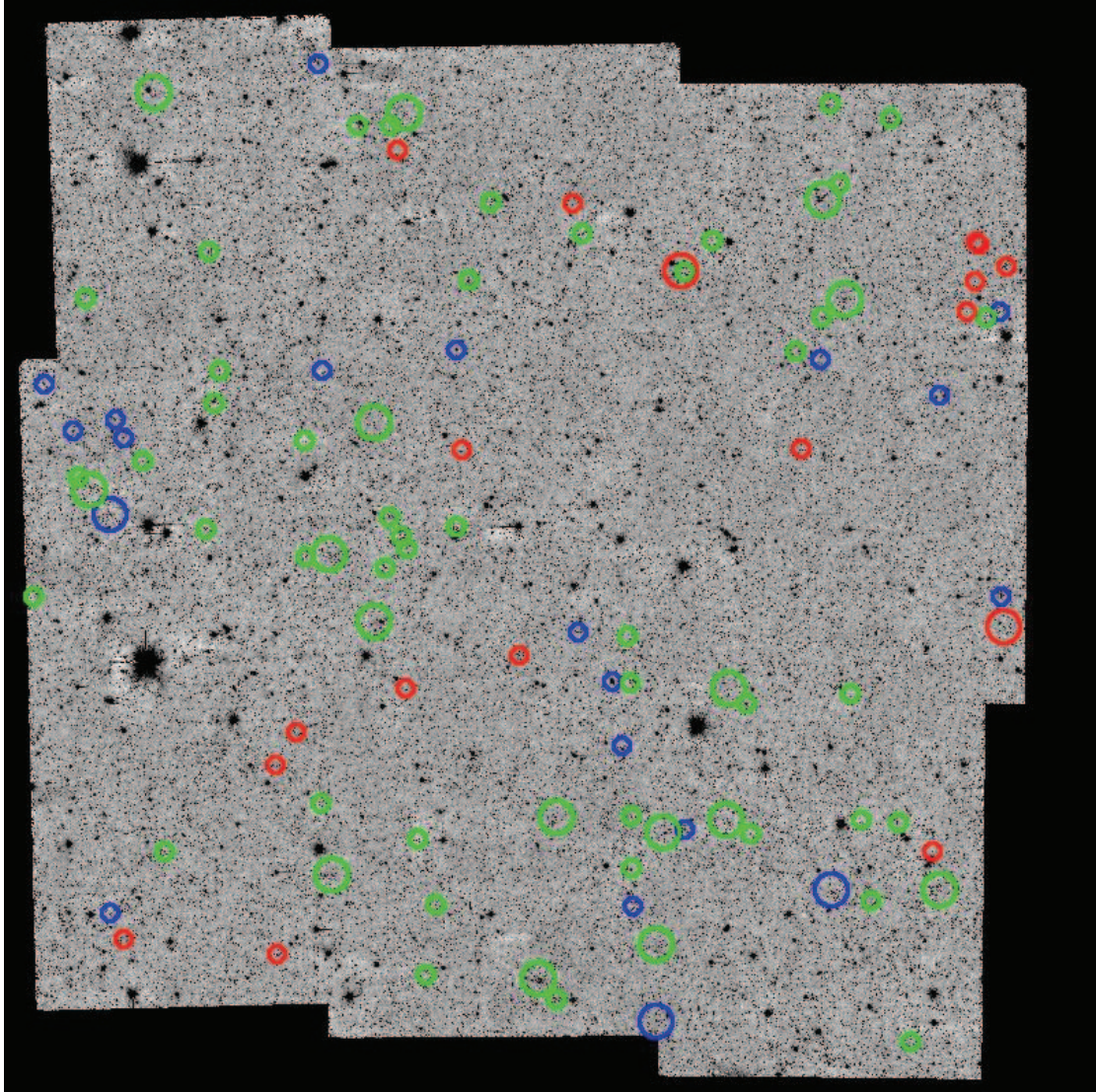


FIG. 5.— The $3.6 \mu\text{m}$ image of the FLS with the positions of clusters superposed. The blue, green, and red circles denote clusters with $0.1 < z < 0.4$, $0.4 < z < 0.8$, and $z > 0.8$, respectively. Large circles represent clusters with $M_{200} > 3 \times 10^{14} M_{\odot}$, and small circles represent clusters with $M_{200} < 3 \times 10^{14} M_{\odot}$. The size of the circles is arbitrarily chosen for clarity and is not related to the projected size of R_{200} for the clusters.

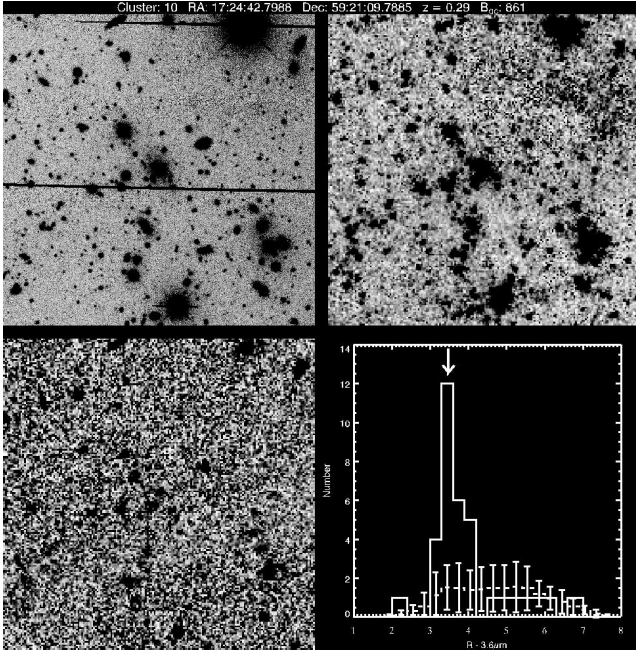


FIG. 6.— Multiwavelength images of FLS J172449+5921.3 at $z_{\text{spec}} = 0.252$ (cluster 10 from Table 1). The top left, top right, and bottom left panels are the R band, IRAC 3.6 μm , and IRAC 8.0 μm , respectively. In each image the field of view is 1 Mpc across at the redshift of the cluster. The solid histogram in the bottom right panel shows the color distribution of galaxies with $M < M^*$ in the same field. The dashed histogram is the background distribution in the same aperture, and the error bars show the average variance in the background. The arrow marks the color of the red sequence from the color-redshift models. The cluster red sequence is clearly detected at many sigma above the background.

green, and red circles, respectively. The clusters themselves are clearly clustered, demonstrating the need for wide-field surveys when searching for representative samples of galaxy clusters.

We show a few examples of some of the richest cluster candidates in Figures 6–11. The top left panel for each figure is the R -band image, the top right panel is the 3.6 μm image, and the bottom left panel is the 8.0 μm image. All images are 1 Mpc across at the cluster redshift. The bottom right panel of each figure shows a histogram of the color distribution of galaxies with $M < M^*$ within a 1 Mpc diameter aperture. The color of the red sequence for the photometric redshift is marked with an arrow. The dashed histogram is the mean color background in that aperture measured from the entire survey. The error bars on the dashed histogram are computed as the 1σ variance in each bin from 200 randomly selected 1 Mpc apertures within the survey. Galaxies are clustered, and therefore assuming that the variance is Gaussian distributed is probably an overestimate of the true variance (because there will be large wings in the distribution due to clustering); however, it provides a first-order demonstration of the overdensity of the cluster relative to the field.

Overall, the cluster catalog is qualitatively similar in both redshift and richness distributions to catalogs selected with the same technique in different bandpasses (e.g., Gladders & Yee 2005; Gilbank et al. 2004), demonstrating that clusters can be reliably selected with the CRS method on IRAC data despite the limited spatial resolution of the instrument.

5. CLUSTER LUMINOSITY FUNCTIONS

In this section we measure the IRAC LFs of the FLS cluster sample and use these to study the evolution of stellar mass assembly and dusty star formation/active galactic nucleus (AGN) activity in clusters.

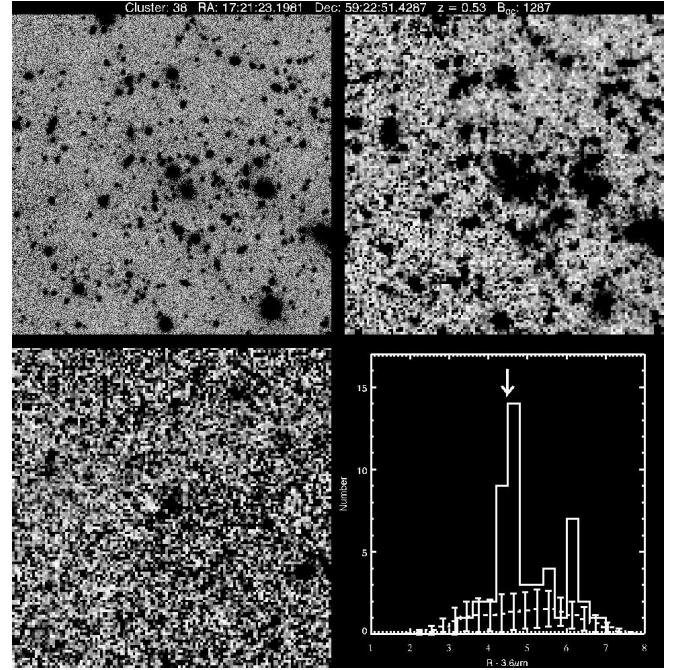


FIG. 7.— Same as for Fig. 6, but for FLS J172122+5922.7 at $z_{\text{phot}} = 0.53$ (cluster 38 from Table 1).

5.1. The 3.6 and 4.5 μm Luminosity Functions

The luminosity of galaxies at 3.6 and 4.5 μm over the redshift range $0.1 < z < 1.5$ is dominated by emission from low-mass stars and is fairly insensitive to ongoing star formation or dust. Consequently, the 3.6 and 4.5 μm cluster LFs provide an estimate of the stellar mass function of cluster galaxies, and their redshift evolution can constrain the mass assembly history of cluster galaxies. One concern with using these LFs as a proxy for the stellar mass function is that at $z < 0.5$ the 3.3 μm PAH feature found in strongly star-forming galaxies can contaminate the

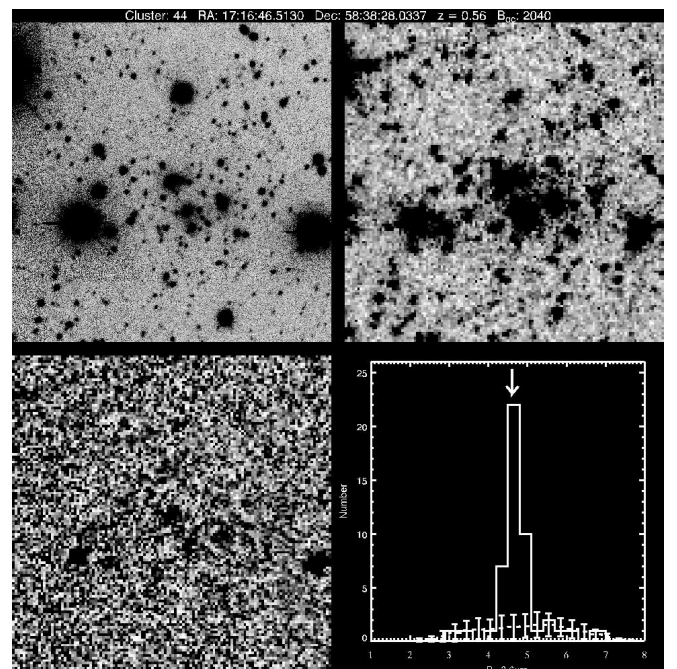


FIG. 8.— Same as for Fig. 6, but for FLS J171648+5838.6 at $z_{\text{phot}} = 0.56$ (cluster 44 from Table 1).

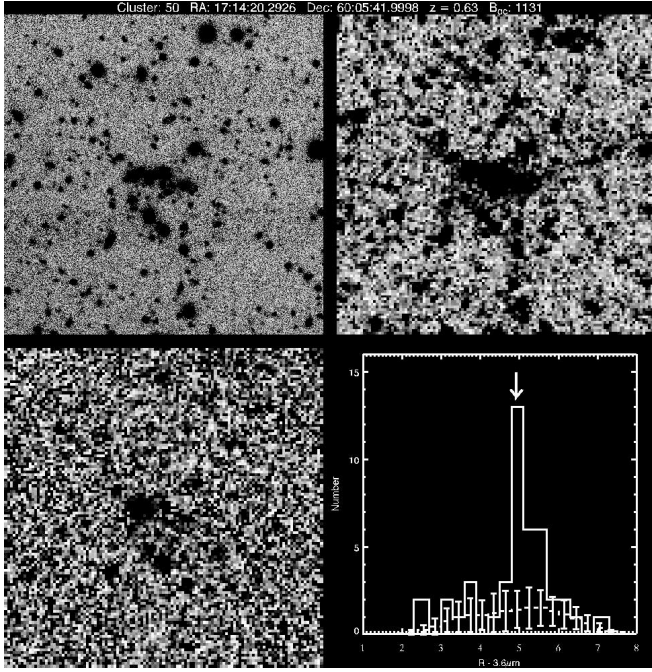


FIG. 9.—Same as for Fig. 6, but for FLS J171420+6005.5 at $z_{\text{phot}} = 0.63$ (cluster 50 from Table 1).

stellar emission observed at 3.6 and 4.5 μm ; however, it is likely that such contamination will be small for cluster galaxies in this redshift range. In a study of luminous infrared galaxies (LIRGs; $L_{\text{IR}} > 10^{11} L_{\odot}$) with estimated SFRs of $\sim 100 M_{\odot} \text{ yr}^{-1}$, Magnelli et al. (2008) found that the excess emission in the IRAC bands due to the 3.3 μm PAH feature was only $\sim 30\%$. Given that such luminous LIRGs are fairly rare at $z < 0.5$ (e.g., Pérez-González et al. 2005) and the increase in flux is small, even for strongly star-forming galaxies, contamination of the 3.6 and 4.5 μm bandpasses by 3.3 μm PAH emission should be negligible.

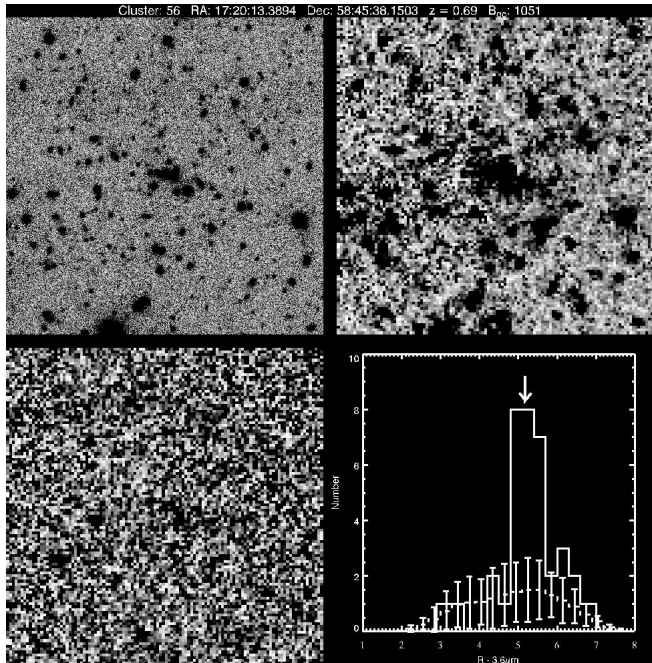


FIG. 10.—Same as for Fig. 6, but for FLS J172013+5845.4 at $z_{\text{phot}} = 0.69$ (cluster 56 from Table 1).

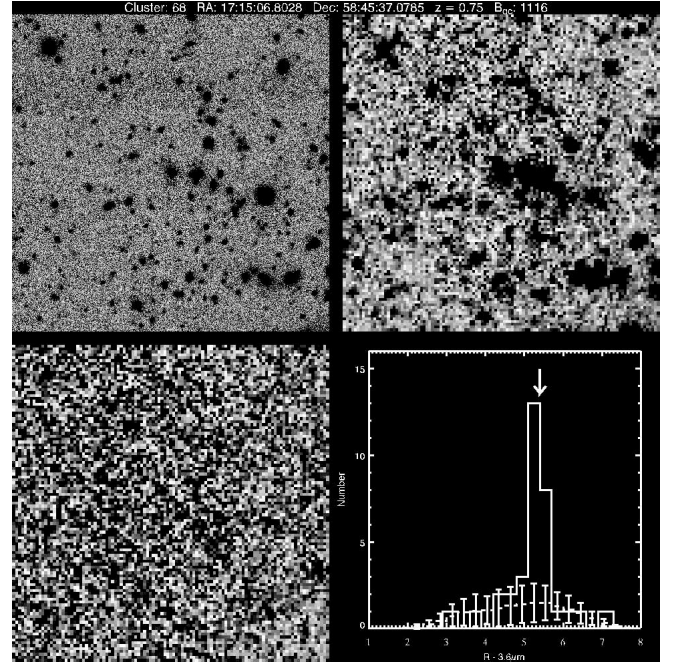


FIG. 11.—Same as for Fig. 6, but for FLS J171508+5845.4 at $z_{\text{phot}} = 0.75$ (cluster 68 from Table 1).

Another concern is that in the worse cases there can be variations in the stellar mass-to-light ratio (M_*/L) of galaxies in similar bandpasses as large as a factor of 5–7 (such as in the K band; e.g., Brinchmann 1999; Bell & de Jong 2001; Bell et al. 2003). These variations are smaller for evolved populations such as those found in clusters, and in general the luminosity of a galaxy at 3.6 and 4.5 μm is still a reasonable proxy for its stellar mass.

Exhaustive studies of both the K -band (e.g., De Propris et al. 1999; Lin et al. 2006; Muzzin et al. 2007a) and 3.6 and 4.5 μm (Andreon 2006; De Propris et al. 2007) LFs of cluster galaxies have shown that the evolution of M^* in these bands is consistent with a passively evolving stellar population formed at high redshift ($z_f > 1.5$), suggesting that the majority of the stellar mass in bright cluster galaxies is already assembled into massive galaxies by at least $z \sim 1$. Here we compute the LFs in the 3.6 and 4.5 μm bands for the FLS clusters to confirm that the FLS cluster sample provides similar results and to demonstrate that these LFs can be used to estimate the stellar contribution to the MIR cluster LFs (§ 5.2).

The LFs are measured by stacking clusters in redshift bins of $\Delta z = 0.1$ starting from $z = 0.1$. For each cluster, the number of galaxies within R_{200} in 0.25 mag bins is tabulated and the expected number of background galaxies within R_{200} is subtracted from these counts. The background counts are determined from the entire 3.8 deg^2 survey area and are well constrained. Each background-subtracted cluster LF is then “redshifted” to the mean redshift of the bin using a differential distance modulus and a differential k -correction determined from the single-burst model (§ 3.1). At 3.6 and 4.5 μm the k -corrections for galaxies are almost independent of spectral type (e.g., Huang et al. 2007); therefore, using only the single-burst k -correction rather than a k -correction based on spectral type does not affect the LFs. Furthermore, the differential k -corrections and distance moduli are small (typically < 0.1 mag) and do not affect the LFs in a significant way.

The final stacked LFs are constructed by summing the individual LFs within each bin. The errors for each magnitude bin of

the final LF are computed by adding the Poisson error of the total cluster counts to the Poisson error of the total background counts in quadrature.

In Figures 12 and 13 we plot the 3.6 and 4.5 μm cluster LFs, respectively. The 3.6 μm LFs are fitted to a Schechter (1976) function of the form

$$\phi(M) = (0.4 \ln 10) \phi_* \left(10^{0.4(M^* - M)} \right)^{1+\alpha} \exp\left(-10^{0.4(M^* - M)}\right), \quad (3)$$

where α is the faint-end slope, ϕ_* is the normalization, and M^* is the “characteristic” magnitude, which indicates the transition between the power-law behavior of the faint end and the exponential behavior of the bright end. The functions are fitted using the Levenberg-Marquardt algorithm for least squares (Press et al. 1992), and errors are estimated from the fitting covariance matrix. The data are not deep enough to provide good constraints on α , ϕ_* , and M^* simultaneously; therefore, the faint-end slopes of the LFs are assumed to be fixed at $\alpha = -0.8$. This value is similar to the $\alpha = -0.84 \pm 0.08$ measured in the K band for clusters at $z \sim 0.3$ by Muzzin et al. (2007a), as well as the value measured in the K band for local clusters ($\alpha = -0.84 \pm 0.02$) by Lin et al. (2004). Although assuming a fixed value of α precludes measuring any evolution of the faint-end slope of the LFs with redshift, it removes the strong correlation between M^* and α in the fitting and, provided that the evolution in α is modest, is the best way to measure the luminosity evolution of the cluster galaxies via the evolution of M^* . The fitted values of M^* and the 1σ errors are listed in the upper left corner of the panels in Figure 12.

We plot the evolution of M^* at 3.6 μm as a function of redshift in Figure 14 as filled circles. Figure 14 also shows the predicted evolution of M^* for single-burst models with $z_f = 1.0, 1.5, 2.0, 2.8$, and 5.0 . These models are normalized to $M^* = -24.02$ at $z = 0$ in the K band, the result obtained by Lin et al. (2004) for 93 local clusters. This corresponds to a normalization of $M^* = -24.32$ at 3.6 μm , assuming a $K - 3.6 \mu\text{m}$ color from the $z_f = 2.8$ passive evolution model. The FLS values of M^* are consistent with most of these models, except the $z_f = 1.0$ model, for which they are clearly too faint. Therefore, similar to the majority of previous studies, we can conclude that the bulk of the stellar mass in bright cluster galaxies is consistent with having been both formed and assembled at $z > 1.5$ and has passively evolved since then. As a comparison, the values measured at 3.6 μm by De Propriis et al. (2007) and Andreon (2006) are overplotted as open squares and open diamonds, respectively. These values are from spectroscopically confirmed samples of ~ 40 clusters (the majority of which are X-ray-detected clusters), and both agree well with the FLS values demonstrating that passive evolution appears to be the ubiquitous conclusion regardless of cluster sample.

Similar to the 3.6 μm LFs, the 4.5 μm LFs can be fitted using a Schechter function; however, we do not perform fitting of the 4.5 μm LFs. Instead, as a demonstration of the technique presented in §§ 5.2.3 and 5.2.4, we use the measured 3.6 μm LFs to predict the 4.5 μm LFs. Unlike colors from the redder IRAC channels, the 3.6 $\mu\text{m} - 4.5 \mu\text{m}$ colors of galaxies are nearly identical for most spectral types over the redshift range $0.1 < z < 1.5$. As a consequence, the 4.5 μm LFs can be predicted from the 3.6 μm LFs using the 3.6 $\mu\text{m} - 4.5 \mu\text{m}$ colors from almost any stellar population model. For simplicity, we use the passive evolution model to predict the 4.5 μm LFs. The inferred 4.5 μm LFs are overplotted as solid lines in Figure 13. The predicted 4.5 μm LFs are consistent with the measured ones, and this demonstrates that

the 3.6 μm LFs combined with simple models for the color evolution of galaxies can predict the LFs in other bandpasses. Furthermore, the self-consistency between the 3.6 and 4.5 μm LFs at $z = 0.15$, where the 3.3 μm PAH would contaminate the 3.6 μm band, and at $z = 0.33$, where it would contaminate the 4.5 μm band, suggests that the primary source of the emission in these bandpasses at $z < 0.5$ is stellar.

5.2. The 5.8 and 8.0 μm Luminosity Functions

Unlike the 3.6 and 4.5 μm bandpasses where the luminosity of galaxies is dominated by emission from low-mass stars, the luminosity of galaxies at 5.8 and 8.0 μm comes from several sources. It can have contributions from warm dust continuum, PAH emission, and low-mass stars. In particular, if warm dust (heated by intense star formation or an AGN) or PAH emission is present, it typically dominates the luminosity at these wavelengths. Therefore, the 5.8 and 8.0 μm LFs can be useful probes of the amount of dusty star formation and AGN activity in clusters if the contribution from stellar emission is properly accounted for.

The main challenge in modeling the LFs at these wavelengths is that a massive, dust-free early-type galaxy produces relatively the same flux at 5.8 and 8.0 μm from pure stellar emission as a much lower mass starburst galaxy or AGN produces from PAH emission or warm dust continuum. Determining the relative abundance of each of these populations in an LF is more challenging for a statistically defined sample such as this cluster sample where individual galaxies are not identified as field/cluster or star-forming/non-star-forming. Despite this challenge, we showed in § 5.1 that the 3.6 μm LFs can be used as a diagnostic of the average stellar emission from the cluster galaxies and that with a model for galaxy colors they can predict the 4.5 μm LFs extremely well. The 3.6 $\mu\text{m} - 5.8 \mu\text{m}$ and 3.6 $\mu\text{m} - 8.0 \mu\text{m}$ colors of different spectral types vary significantly more than the 3.6 $\mu\text{m} - 4.5 \mu\text{m}$ colors; however, if these colors are modeled correctly, the same technique can be used to model the LFs in the 5.8 and 8.0 μm bandpasses and provide constraints on the number and type of star-forming galaxies in clusters.

Put another way, the 3.6 μm LF provides effectively a “stellar mass budget” for predicting the 5.8 and 8.0 μm LFs. Subtracting this stellar mass budget at 5.8 and 8.0 μm leaves an excess that can be modeled with different populations of star-forming galaxies or AGNs. Unfortunately, such models are unlikely to be completely unique in the sense that there will be a degeneracy between the *fraction* of star-forming galaxies or AGNs and the *intensity* of the star formation or AGN activity within those galaxies; however, we show that using only rough empirical constraints on the fraction of star-forming/non-star-forming galaxies in clusters places interesting constraints on the intensity of star formation in cluster galaxies and the relative percentages of “regular” star-forming galaxies and dusty starbursts.

5.2.1. Measuring the 5.8 and 8.0 μm Luminosity Functions

Before models of the cluster population are made, we measure the 5.8 and 8.0 μm LFs using the same stacking and background subtraction methods as for the 3.6 and 4.5 μm LFs. The LFs are plotted in Figures 15 and 16 in the same redshift bins as the 3.6 and 4.5 μm LFs. IRAC is significantly less sensitive at 5.8 and 8.0 μm than at 3.6 and 4.5 μm and therefore these LFs are much shallower. Only the bright end of the LF (roughly $M < M^*$, assuming a dust-free, pure stellar emission early-type model) can be measured with these data; however, this shallow depth is still sufficient to be a good diagnostic of the presence of luminous dusty starbursts. For example, at $0.1 < z < 0.4$, an M82-type starburst

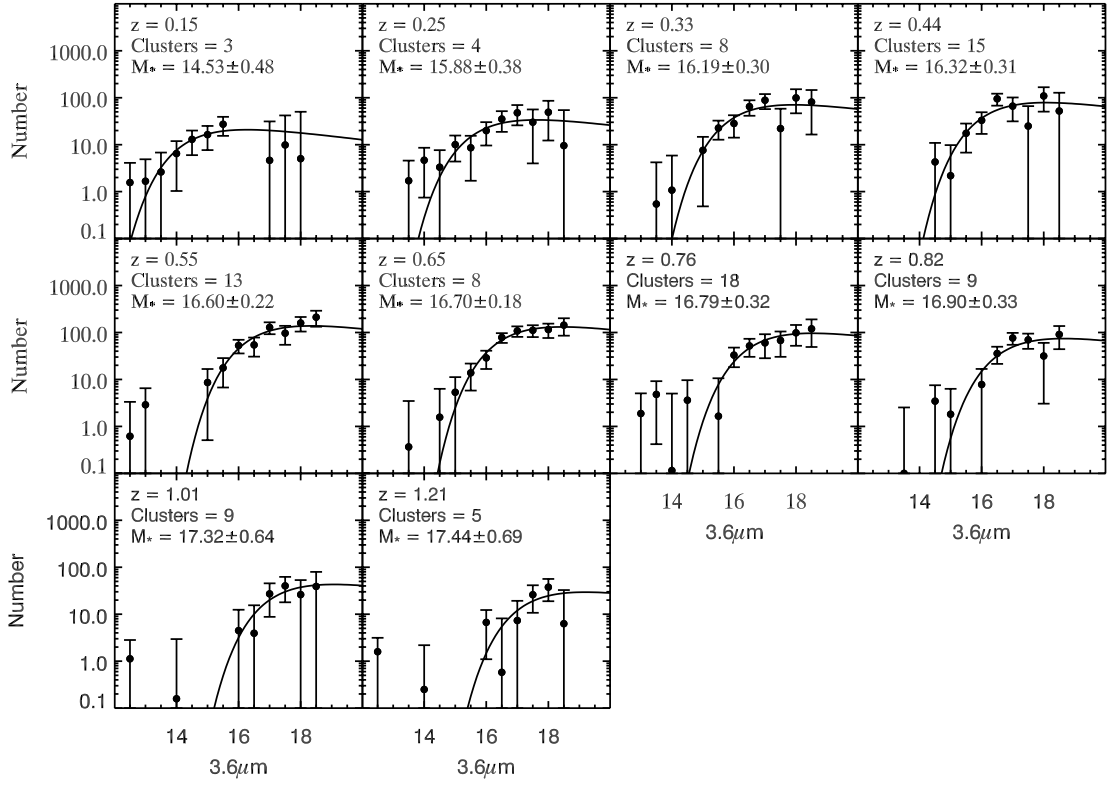


FIG. 12.— The 3.6 μm LFs of clusters in the FLS. The solid line shows the best-fit Schechter function assuming $\alpha = -0.8$. The redshift, the value of M_* , and the number of clusters combined to make the LF are listed in the upper left corner of each panel.

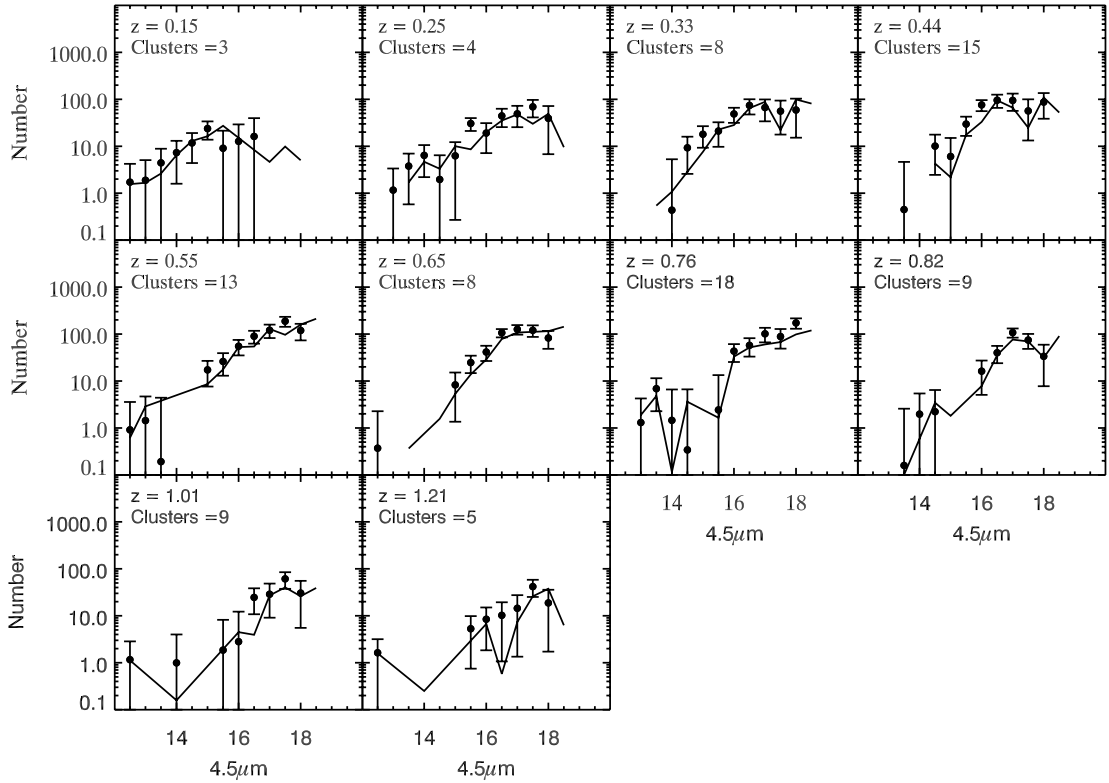


FIG. 13.— The 4.5 μm LFs of clusters in the FLS in the same redshift bins as Fig. 12. The solid line is the 4.5 μm LF that is predicted from the 3.6 μm LF assuming that galaxies have the 3.6 $\mu\text{m} - 4.5 \mu\text{m}$ colors of a passively evolving population formed at high redshift.

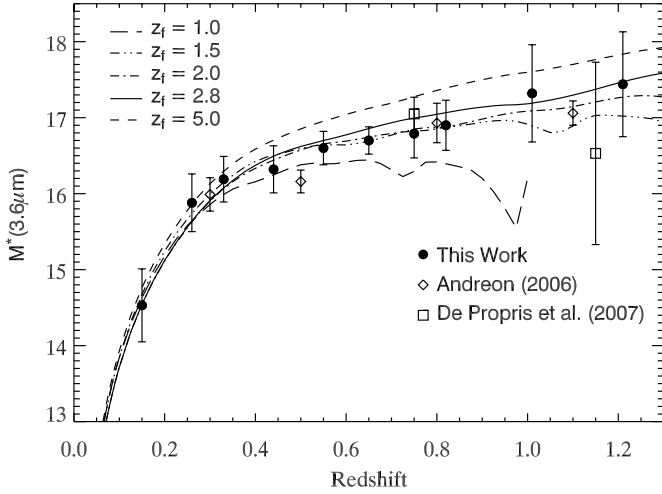


FIG. 14.— Evolution in M^* from the $3.6\ \mu\text{m}$ LFs as a function of redshift. The long-dashed, triple-dot-dashed, dot-dashed, solid, and short-dashed lines show models where the stars form in a single burst at $z = 1.0, 1.5, 2.0, 2.8$, and 5.0 , respectively. The filled circles are the FLS clusters, and the open diamonds and open squares are the M^* values from the Andreon (2006) and De Propriis et al. (2007) cluster samples, respectively.

is roughly 3 mag brighter at $8.0\ \mu\text{m}$ than an early-type model (e.g., Huang et al. 2007; Wilson et al. 2007; see also § 6.3); therefore, even a galaxy with $M \sim M^* + 3$ from the $3.6\ \mu\text{m}$ LF would be detected at $8.0\ \mu\text{m}$ if undergoing an M82-like dusty starburst.

5.2.2. Contamination from AGNs

In order to draw conclusions from models of the MIR cluster LFs, it is important to have some constraints on the fraction of cluster MIR sources that are AGNs and the fraction that are star-forming galaxies. The fraction of galaxies in clusters at $z < 0.6$ identified as AGNs based on their optical spectra in clusters is low ($< 2\%$; e.g., Dressler et al. 1985, 1999), whereas the fraction of star-forming galaxies can be quite large (5%–80%; e.g., Butcher & Oemler 1984; Dressler et al. 1999; Ellingson et al. 2001; Poggianti et al. 2006). Therefore, it might be expected that star-forming galaxies will dominate the overall number of cluster MIR sources. It is possible that the AGN fraction in clusters may have been underestimated because some cluster AGNs are missed by optical selection. X-ray observations of moderate-redshift clusters have found an additional population of cluster X-ray AGNs that do not have AGN-like optical spectra (e.g., Martini et al. 2006, 2007; Eastman et al. 2007). Martini et al. (2007) showed that this population is roughly as large as the optical AGN population, making the overall AGN fraction $\sim 5\%$ for cluster galaxies at $z \sim 0.2$ with moderate-luminosity AGNs (broadband X-ray luminosities $L_X > 10^{41}\ \text{ergs s}^{-1}$), but only $\sim 1\%$ for those with bright AGNs ($L_X > 10^{42}\ \text{ergs s}^{-1}$). If the analysis is restricted to galaxies with hard X-ray luminosities $> 10^{42}\ \text{ergs s}^{-1}$, then the fraction is about an order of magnitude lower (0.1%; Eastman et al. 2007).

Although these studies suggest that the AGN fraction in clusters is low, particularly for bright AGNs, it is unclear how many of the optical- and X-ray-selected cluster AGNs will have detectable MIR emission, and what fraction of the cluster MIR population they comprise. Previous MIR studies of clusters have detected only a few AGNs in spectroscopic samples of ~ 30 –80 cluster MIR sources (e.g., Duc et al. 2002; Coia et al. 2005; Marcillac et al. 2007; Bai et al. 2007), suggesting that $> 90\%$ of cluster galaxies detected in the MIR are star-forming galaxies.

One way to estimate the fraction of cluster MIR-bright AGNs is to use the IRAC and MIPS color-color diagrams suggested by Lacy et al. (2004) and Stern et al. (2005). Although these simple color cuts fail to identify complete samples of AGNs because they only identify those that have red power-law slopes in the MIR (e.g., Cardamone et al. 2008), these are precisely the type of AGNs that will be included in the 5.8 and $8.0\ \mu\text{m}$ LFs and therefore the color cuts should provide a reasonable estimate of the contamination of those LFs from AGNs.

In the left panels of Figure 17 we plot the IRAC colors of all galaxies brighter than the 50% completeness limits using the color spaces suggested by Stern et al. (2005) (*top left panel*) and Lacy et al. (2004) (*bottom left panel*). The dashed lines in each panel represent the portion of color space used to select AGNs in the MIR by these authors. FLS galaxies that satisfy the color criteria are plotted as gray circles. The right panels of Figure 17 show the same plots for all galaxies with $R < R_{200}$ for clusters at $z < 0.7$ in the FLS (59 clusters).

The entire FLS (*left panels*) can be used to estimate the surface density of MIR-selected AGNs in these color spaces. Subtracting this background from the cluster fields, we find an excess of 26 ± 22 galaxies using the Stern et al. (2005) color cut and an excess of 30 ± 30 galaxies using the Lacy et al. (2004) color cut. Summing the background-subtracted $3.6\ \mu\text{m}$ LFs to the same limit implies that there are 2466 total cluster galaxies in these 59 clusters and that the overall fraction of cluster galaxies that are candidate MIR-bright AGNs (to our $3.6\ \mu\text{m}$ detection limit) is $1^{+1}_{-1}\%$, where all error bars have been calculated using Poisson statistics. Integrating the 5.8 and $8.0\ \mu\text{m}$ LFs shows that there are 869 and 959 cluster galaxies detected in these bands and that the fraction of cluster sources detected in the MIR that are candidate AGNs is $\sim 3^{+3}_{-3}\%$.

Although this crude estimate is almost certainly an incomplete census of the total fraction of AGNs in clusters, it is remarkably similar to the AGN fractions measured with optical spectroscopy or by X-ray selection and is consistent with the fraction of spectroscopically confirmed MIR-bright AGNs seen in previous cluster MIR studies. Based on the low estimated AGN fraction, and for the sake of simplicity in interpretation, we do not model an AGN component in the 5.8 and $8.0\ \mu\text{m}$ LFs in this analysis. We do note that the X-ray, spectroscopic, and MIR selections do show clearly that the fraction of MIR cluster sources that are AGNs is *not* zero, and therefore some of the sources in the 5.8 and $8.0\ \mu\text{m}$ LFs will certainly be AGNs.

5.2.3. Modeling the $5.8\ \mu\text{m}$ Luminosity Function

The simplest fiducial model that can be made for the MIR cluster galaxy population is to assume that the bright end of the LF is dominated by passive, dust-free, early-type galaxies (i.e., the emission at 5.8 and $8.0\ \mu\text{m}$ is completely stellar). Although such a model is unrealistic, it provides a baseline for predicting the amount of emission in the MIR from stellar emission, and any excess beyond this model is likely to be from dusty star formation in the cluster population. Assuming such a model, the $5.8\ \mu\text{m}$ LFs can be inferred from the $3.6\ \mu\text{m}$ LFs using the $3.6\ \mu\text{m} - 5.8\ \mu\text{m}$ colors from the Bruzual & Charlot passive evolution model. These predicted $5.8\ \mu\text{m}$ LFs are overplotted on the LFs in Figure 15 as the solid red lines (Fig. 15 also has additional models overplotted that are introduced in § 5.2.4).

Qualitatively, the $3.6\ \mu\text{m}$ LFs and the passive evolution model predict the $5.8\ \mu\text{m}$ LFs reasonably well at all redshifts. This is perhaps not surprising because, due to k -corrections, $5.8\ \mu\text{m}$ is only sensitive to emission from warm dust or PAHs in star-forming galaxies at $z < 0.3$ (see § 6.3). For galaxies at higher redshift,

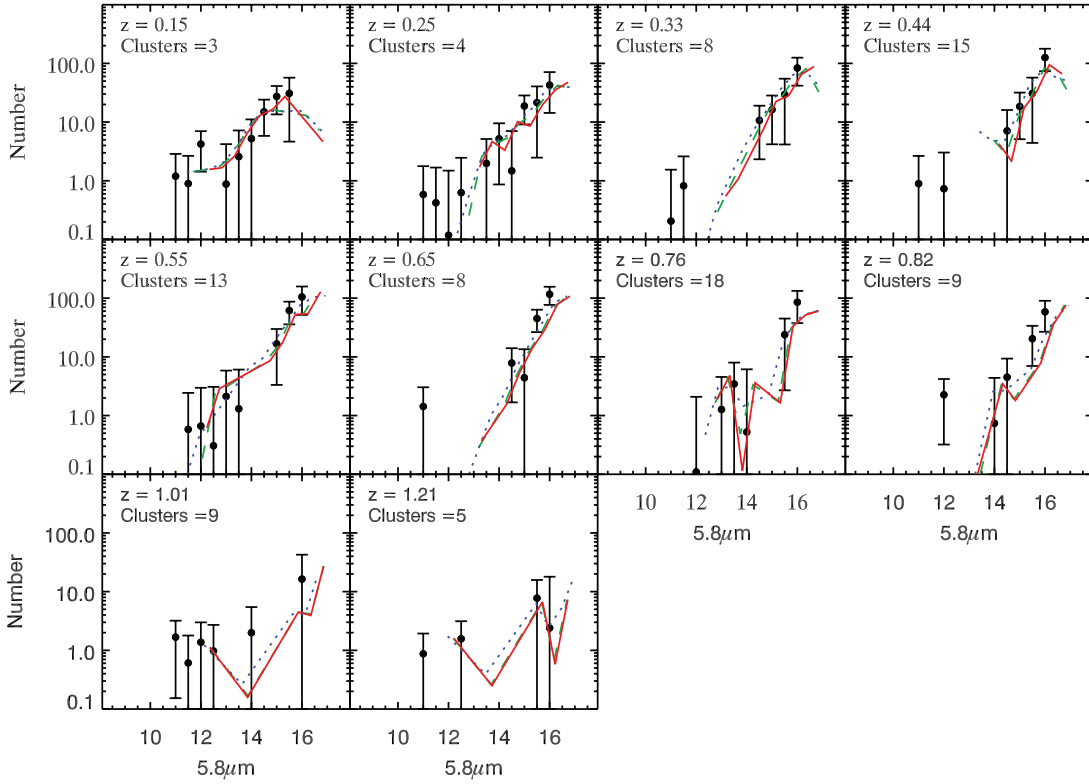


FIG. 15.— The $5.8 \mu\text{m}$ LF of clusters in the FLS. The solid red line shows the $5.8 \mu\text{m}$ predicted from the $3.6 \mu\text{m}$ LF assuming that all galaxies have the colors of the passive evolution model. The dashed green lines and dotted blue lines are the regular+quiescent and starburst+regular+quiescent models described in § 5.2.4, respectively; however, $5.8 \mu\text{m}$ is not sensitive to PAH emission or warm dust at $z > 0.3$ and therefore these models are not notably different from the passive evolution model.

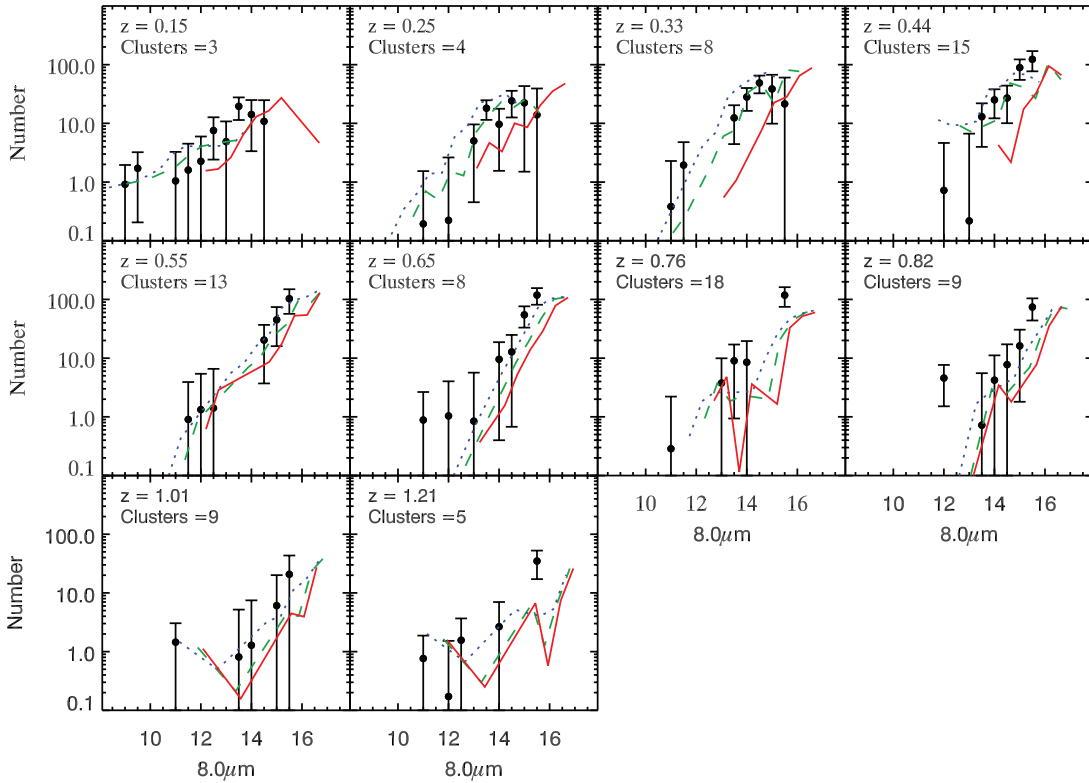


FIG. 16.— The $8.0 \mu\text{m}$ LF of clusters in the FLS. The solid red line, dashed green line, and dotted blue line are the $8.0 \mu\text{m}$ LF predicted using the $3.6 \mu\text{m}$ LF and the quiescent, regular+quiescent, and starburst+regular+quiescent models, respectively, described in § 5.2.4. At lower redshift ($z < 0.4$) the LF is most similar to the predictions from the regular+quiescent model, whereas at higher redshift ($z > 0.4$) the LF is better described by the starburst+regular+quiescent model.

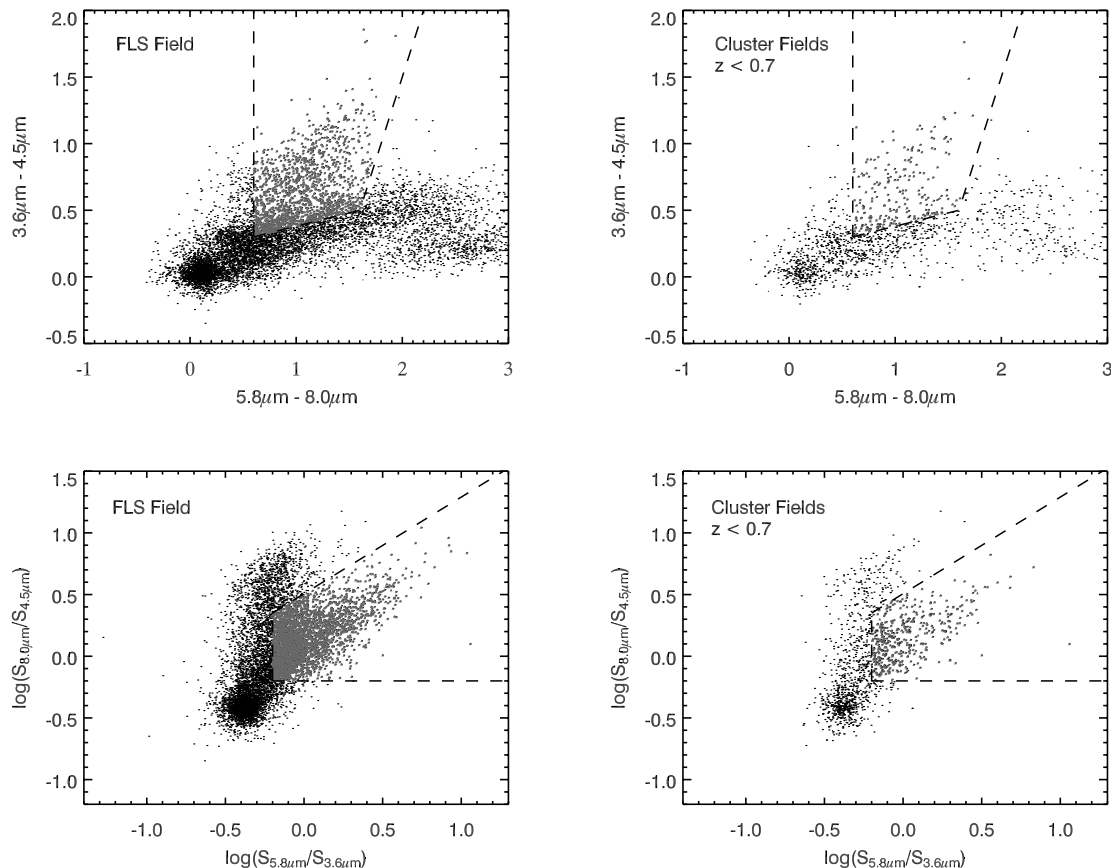


FIG. 17.— *Top left:* Color-color plot of all galaxies in the FLS (*small circles*). The dashed lines denote the region used to select AGNs by Stern et al. (2005). *Bottom left:* Same as the top left panel, but for the Lacy et al. (2004) color space. *Right panels:* Color-color plots for galaxies at $R < R_{200}$ in the fields of clusters at $z < 0.7$ (59 clusters). The majority of these sources are foreground or background galaxies. Background subtraction based on the surface density of sources in the left panels suggests that 1^{+1}_{-1} % of cluster galaxies detected at $3.6 \mu\text{m}$ are AGNs and that $\sim 3^{+3}_{-3}$ % of cluster galaxies detected at 5.8 and $8.0 \mu\text{m}$ are AGNs.

$5.8 \mu\text{m}$ probes rest-frame wavelengths that, similar to the $3.6 \mu\text{m}$ LFs, are dominated by stellar emission. As a result, any dusty star-forming cluster galaxies would only be visible as a notable excess in the predicted $5.8 \mu\text{m}$ LFs at $z < 0.3$. No such excess is seen; however, the fraction of blue star-forming galaxies in clusters evolves rapidly (i.e., the Butcher-Oemler effect), and clusters at $z < 0.3$ typically have low blue fractions and relatively few star-forming galaxies (e.g., Ellingson et al. 2001; Balogh et al. 1999; Margoniner et al. 2001). This result confirms that the fraction of star-forming galaxies in clusters at $z < 0.3$ is low and that, furthermore, there is no significant additional population of MIR-luminous dusty star-forming galaxies in clusters at these redshifts that are missing from optically selected spectroscopic or photometric studies.

5.2.4. Modeling the $8.0 \mu\text{m}$ Luminosity Function

Unlike the $5.8 \mu\text{m}$ LFs, the cluster $8.0 \mu\text{m}$ LFs are not consistent with the passive evolution model predictions from the $3.6 \mu\text{m}$ LFs illustrated by the solid red lines plotted in Figure 16. This model clearly underpredicts the number of galaxies in the $8.0 \mu\text{m}$ LFs at all redshifts.

In order to construct a more useful model for the $8.0 \mu\text{m}$ LF that includes the cluster star-forming population, we use the $3.6 \mu\text{m} - 8.0 \mu\text{m}$ colors for different types of star-forming galaxies from J. Huang et al. (2008, in preparation). These authors have empirically extended the color/redshift models of Coleman et al. (1980) to $10 \mu\text{m}$ using local galaxies with *ISO* spectroscopy.

Some examples of the colors from these models are presented in Wilson et al. (2007).

Given the large number of permutations possible in the types of star-forming galaxies, we are interested in as simple a model as possible that will allow for a straightforward interpretation of the data. For this analysis we divide the cluster star-forming population into two populations: “regular” star-forming cluster spirals, and dusty starburst galaxies. J. Huang et al. (2008, in preparation) have models for both Sbc and Scd galaxies; however, the $3.6 \mu\text{m} - 8.0 \mu\text{m}$ colors of these models are indistinguishable, and therefore we adopt their Sbc galaxy as the model for a “regular” star-forming cluster spiral. J. Huang et al. (2008, in preparation) also have colors for several “canonical” dusty starburst galaxies such as M82, Arp 220, and NGC 1068. M82 is a moderate-strength dusty starburst, has no AGN component, and is classified as an LIRG. By contrast, Arp 220 and NGC 1068 are powerful dusty starbursts with AGN components. The IR luminosity of Arp 220 is dominated by star formation from a major merger, while the IR luminosity of NGC 1068 is dominated by a powerful AGN (although both galaxies have AGN and starburst components). Both are classified as ultraluminous infrared galaxies (ULIRGs). Given that the majority of distant clusters studied thus far in the MIR have shown a significant population of LIRGs but no population of ULIRGs (e.g., Coia et al. 2005; Geach et al. 2006; Marcillac et al. 2007), we assume that any cluster dusty starbursts will have colors similar to M82, rather than Arp 220 or NGC 1068. In general, replacing M82 as the model for cluster dusty

starbursts with either Arp 220 or NGC 1068 requires a smaller fraction of dusty starbursts since they are more luminous.

In order to ascertain the dominant mode of star formation present in the cluster population, we can construct simple models for the 8.0 μm LFs from the 3.6 μm LFs using various combinations of these populations. The purpose of the models is not to perfectly reproduce the cluster 8.0 μm LFs (this requires a much more detailed knowledge of the populations in each cluster than can be obtained by statistical background subtraction), but to demonstrate how the 8.0 μm LFs should appear given different proportions of these populations and thereby estimate the importance of the contribution of each to the 8.0 μm LFs. Hereafter we refer to the Sbc model as “regular,” the M82 model as “dusty starburst,” and the Bruzual & Charlot passive evolution model as “quiescent.”

Beyond assuming that all cluster galaxies are quiescent, which clearly underpredicts the 8.0 μm LFs, the next most simple model that can be made is to assume that some fraction of the cluster galaxies are regular star-forming galaxies (hereafter we refer to this model as regular+quiescent). In order to make such a model, we require an approximation of the relative proportions of star-forming and quiescent galaxies in clusters as a function of redshift and luminosity. The best spectroscopically classified data at these redshifts come from the MORPHS (Dressler et al. 1999; Poggianti et al. 1999) and CNOC1 (Balogh et al. 1999; Ellingson et al. 2001) projects. Unfortunately, the number of cluster spectra per dz is relatively small in these samples, and they cover only a modest range in redshift ($0.2 < z < 0.5$) and depth in terms of the cluster M^* .

Although spectroscopic classification would be the most reliable, the lack of data motivates the use of cluster blue fractions (f_b) as a function of redshift as a model for the relative fractions of star-forming/non-star-forming galaxies. Blue fractions for reasonably large samples of clusters at different redshifts have been calculated, and it is fairly straightforward to measure them as a function of magnitude within these clusters. In particular, using f_b as an estimate of the star-forming fraction should predict the number of blue star-forming galaxies (i.e., those with colors similar to the Sbc model). If a population of red, dust-obscured starburst galaxies exists in clusters, they should be evident in the 8.0 μm LFs as an excess of galaxies beyond the regular+quiescent model.

For f_b as a function of redshift we use the data of Ellingson et al. (2001) from the CNOC1 clusters that span the redshift range $z = 0.2$ – 0.4 , and for clusters at $z > 0.4$ we use the data on RCS-1 clusters from Loh et al. (2008). Rough f_b values for both these samples were recomputed using only galaxies with $M < M^*$ (D. Gilbank 2007, private communication) because this matches the depth of the 5.8 and 8.0 μm LFs. These f_b values as a function of redshift are listed in Table 2.

The scatter in cluster f_b values at a given redshift is large; therefore, different studies find different mean values depending on the sample. The values we have adopted are consistent with the majority of work in the field (e.g., Butcher & Oemler 1984; Smail et al. 1998; Margoniner et al. 2001; Andreon et al. 2004), although we have measured them using a brighter luminosity cut. Of course, the best way to infer the f_b of the FLS clusters would be to measure it from the clusters themselves; however, we do not have the proper filter coverage at $z < 0.5$ to make this measurement properly nor a large enough sample to make a measurement that would be statistically different from the adopted values.

The cluster f_b is also a function of limiting magnitude (e.g., Ellingson et al. 2001), and without incorporating some variation

TABLE 2
ASSUMED BLUE FRACTIONS

z (1)	$F_b (M < M^*)$ (2)
0.15.....	0.05
0.25.....	0.15
0.33.....	0.20
0.44.....	0.25
0.55.....	0.30
0.65.....	0.40
0.76.....	0.50
0.82.....	0.50
1.01.....	0.60
1.21.....	0.60

in f_b as a function of magnitude, all of the model LFs consistently overpredict the number of bright galaxies in the 8.0 μm LFs and underpredict the number of faint ones. In order to estimate the variation of f_b as a function of magnitude, we use the spectrally typed LFs of Muzzin et al. (2007a). They measured the K -band LF for cluster galaxies defined spectroscopically as either star-forming or quiescent. Comparing those LFs (their Fig. 13) and assuming that all star-forming galaxies are blue and all quiescent galaxies are red results in f_b values of 0.19, 0.35, and 0.52 for galaxies with $M < M^*$, $M^* < M < M^* + 1$, and $M^* + 1 < M < M^* + 2$, respectively, in clusters at $z \sim 0.3$. Comparing these values shows that f_b is 1.8 times larger at $M^* < M < M^* + 1$ than at $M < M^*$ and is 2.7 times larger at $M^* + 1 < M < M^* + 2$ than at $M < M^*$. We therefore adopt an f_b that varies with magnitude with the following conditions: for galaxies with $M < M^*$ in the 3.6 μm LF we use the f_b values from Table 2, for galaxies with $M^* < M < M^* + 1$ we assume that f_b is twice as large as the values in Table 2, and for galaxies with $M^* + 1 < M < M^* + 2$ we assume that f_b is 3 times as large as the values in Table 2. In cases where this causes $f_b > 1.0$, it is set equal to 1.0.

Combining the f_b as a function of redshift and magnitude with the 3.6 μm LFs assuming that all “blue” galaxies have the color of the J. Huang et al. (2008, in preparation) Sbc galaxies and all “red” galaxies have the color of the passive evolution model results in the models that are plotted as green dashed lines in Figures 15 and 16.

Comparing the data to these models shows that this simple model using only regular+quiescent galaxies predicts the cluster 8.0 μm LFs fairly well. In particular, the $z = 0.15$, 0.25, and 0.33 LFs are well described by this model. For the higher redshift LFs this model is clearly better than the purely quiescent model; however, it still does not account for the entire 8.0 μm population.

Most importantly, the regular+quiescent model shows that out to $z \sim 0.65$, where 8.0 μm still probes rest-frame dust emission, there is no significant population of bright ($M < M^*$) galaxies in clusters that cannot reasonably be accounted for by “regular” star-forming cluster spirals. This is significant because it suggests that whatever processes responsible for transforming the morphology and spectral type of bright cluster galaxies over the same redshift range do not involve an ultraluminous dusty starburst phase such as those caused by major mergers of gas-rich galaxies (i.e., “wet” mergers). We note that there appears to be an over-density of very bright galaxies in the $z = 0.82$ LF that cannot be accounted for by the regular+quiescent model, and this suggests the possibility of an onset of luminous starbursts (possibly from mergers) or AGN activity in bright galaxies at higher redshift.

Although the regular+quiescent model predicts the bright end of the $8.0\ \mu\text{m}$ LFs well at all redshifts and the entire $8\ \mu\text{m}$ LF at lower redshift, it fails to account for all of the LFs. In particular, this model seems to underpredict the number of fainter galaxies in the $8.0\ \mu\text{m}$ LFs for clusters at $z > 0.4$. This suggests a third component to the cluster $8.0\ \mu\text{m}$ population, possibly a red, dusty starburst population that is not accounted for by the cluster f_b . Such a population was suggested by Wolf et al. (2005), who found that the spectral energy distributions of roughly 30% of the red-sequence galaxies in the Abell 901/902 supercluster ($z = 0.17$) were better described by dusty templates rather than a dust-free, old stellar population. In order to explore this possibility, we construct a new model with the same values of f_b as a function of magnitude and redshift as for the regular+quiescent model, but this time we assume that some of the red quiescent galaxies are instead M82-like dusty starbursts. M82 has optical–IR colors that are similar to quiescent galaxies (see J. Huang et al. 2008, in preparation; § 6.3), so it is reasonable to assume that any M82-like dusty starbursts would be part of the population of red cluster galaxies rather than the blue cluster galaxies.

If we assume that the dusty starburst population is a constant fraction of the red cluster galaxies, this would result in a varying ratio of dusty starburst to regular star-forming galaxies in clusters as a function of redshift. In particular, clusters at low redshift will have the highest fraction of dusty starburst galaxies (because the f_b is low and the red fraction is high). The LFs above have already suggested that there is no need for a dusty starburst population at low redshift, so modeling the dusty starbursts as a fixed fraction of the red galaxies seems inappropriate. Instead, a better way to model the population is to assume that the cluster f_b is a tracer of the total star formation in the cluster and that the ratio of dusty starburst to regular star-forming galaxies is a constant. Given this assumption, we can predict the fraction of dusty starbursts directly from the cluster f_b . This fraction of dusty starbursts is then removed from the fraction of red quiescent galaxies, and a model for the LFs can be made. Hereafter we refer to this model as starburst+regular+quiescent. The fractions of the cluster galaxy populations in terms of f_b are defined using the equations

$$f_{\text{dsb}} = f_b \times f_{\text{dsb/reg}}, \quad (4)$$

$$f_q = 1 - f_b - f_{\text{dsb}}, \quad (5)$$

where f_{dsb} is the fraction of dusty starburst galaxies, $f_{\text{dsb/reg}}$ is the assumed ratio of dusty starburst to regular star-forming galaxies, and f_q is the fraction of quiescent galaxies. In cases where $f_{\text{dsb}} + f_b > 1$ we set $f_{\text{dsb}} = 1 - f_b$ and $f_q = 0$.

As of yet there are no good observational constraints on the parameter $f_{\text{dsb/reg}}$. Therefore, as a first-order fiducial value we assume that $f_{\text{dsb/reg}} = 0.5$. In general, we find that allowing a range of values between 0.3 and 1.0 provides models that are fairly similar. More importantly, the differences in models that use $f_{\text{sb/reg}}$ between 0.3 and 1.0 are much smaller than the difference between any of those models and the regular+quiescent model. Therefore, the interpretation of the data using these models will not depend strongly on the assumed value of $f_{\text{sb/reg}}$. The starburst+regular+quiescent model with $f_{\text{sb/reg}} = 0.5$ is overplotted on Figures 15 and 16 as the dotted blue line.

This starburst+regular+quiescent model overpredicts the number of bright galaxies in the $z < 0.4$ $8.0\ \mu\text{m}$ LFs, but it is better at describing the LFs at $z > 0.4$ than the regular+quiescent or purely quiescent models. This suggests that there is a population of dusty

starbursts in clusters at $z > 0.4$ that does not exist at $z < 0.4$ and that these starbursts are consistent with being of an M82 type. We discuss this in more detail in § 6.1.

6. DISCUSSION

6.1. Evidence for a Change in Star Formation Properties of Cluster Galaxies?

In order to better illustrate the differences in the model populations described above, we subtract the quiescent model from the 5.8 and $8.0\ \mu\text{m}$ LFs between $0.15 < z < 0.65$ and plot the residuals in Figures 18 and 19. The residuals from the quiescent+regular and starburst+regular+quiescent models from § 5.2.4 are also plotted in Figures 18 and 19. The solid vertical lines in the plots represent the magnitude of M^* inferred from the $3.6\ \mu\text{m}$ LF assuming the passive evolution model, and they give some indication of the depth of the LFs.

If we compare the data to the models and take the results at face value, it suggests that the intensity of star formation in clusters is evolving with redshift and that it can be classified into three types. The first type of star formation is “weak” and best describes the lowest redshift clusters ($z < 0.15$), which are consistent with the colors of an almost exclusively quiescent population in all IRAC bandpasses. This result is consistent with numerous studies of nearby clusters using spectroscopy that show few star-forming galaxies (e.g., Dressler et al. 1985; Popesso et al. 2007; Christlein & Zabludoff 2005; Rines et al. 2005).

Between $0.2 < z < 0.5$ the $8.0\ \mu\text{m}$ LFs are no longer well described by the purely quiescent model and the regular+quiescent model is the best model. This shows that the majority of star formation in clusters at this epoch is primarily relegated to galaxies that have MIR colors similar to local late-type star-forming galaxies (i.e., the Sbc model). This has direct implications for the SFRs of these galaxies because Wu et al. (2005) showed that the dust-obscured SFR of galaxies is proportional to their $8.0\ \mu\text{m}$ flux. Although other authors have demonstrated that there are caveats when using the $8.0\ \mu\text{m}$ flux to infer SFRs (i.e., the scatter can be as high as a factor of 20–30; Dale et al. 2005), this still implies that the average SFR or the average SFR per unit stellar mass (the average specific star formation rate [SSFR]) of star-forming cluster galaxies at $0.2 < z < 0.5$ is similar to those in the local universe (because they have $3.6\ \mu\text{m} - 8.0\ \mu\text{m}$ colors similar to local Sbc galaxies). This second mode of star formation in clusters is roughly what would be considered regular star formation for galaxies in the local universe.

At $z > 0.5$ the starburst+regular+quiescent model becomes the best description of the LFs. Again, assuming that $8.0\ \mu\text{m}$ flux is an indicator of SFR, the M82 starburst model is approximately a factor of 2.5 brighter at $8.0\ \mu\text{m}$ than the regular Sbc model for the same $3.6\ \mu\text{m}$ flux. Given that our model suggests that regular star-forming galaxies make up $\sim 30\%$ – 40% of the cluster population at this redshift and M82 galaxies make up $\sim 15\%$ – 20% , this implies that not only is the abundance of star-forming galaxies in clusters higher at higher redshift (i.e., the Butcher-Oemler effect), but also the average SSFR of cluster galaxies is approximately a factor of 1.5 higher at $z > 0.5$ than it is at $z < 0.5$. This increase in SSFR suggests a third mode of star formation in cluster galaxies that could be considered a “burst” mode, at least relative to local SFRs. Interestingly, this increase in the SSFR of cluster galaxies at higher redshift is consistent with field studies of the universal star formation density (ρ_*), which show an increase of roughly a factor of 2–5 between $z = 0.2$ and 0.5 (e.g., Lilly et al. 1996; Wilson et al. 2002; Schiminovich et al. 2005; Le Floc’h et al. 2005). It suggests that the increasing fraction of

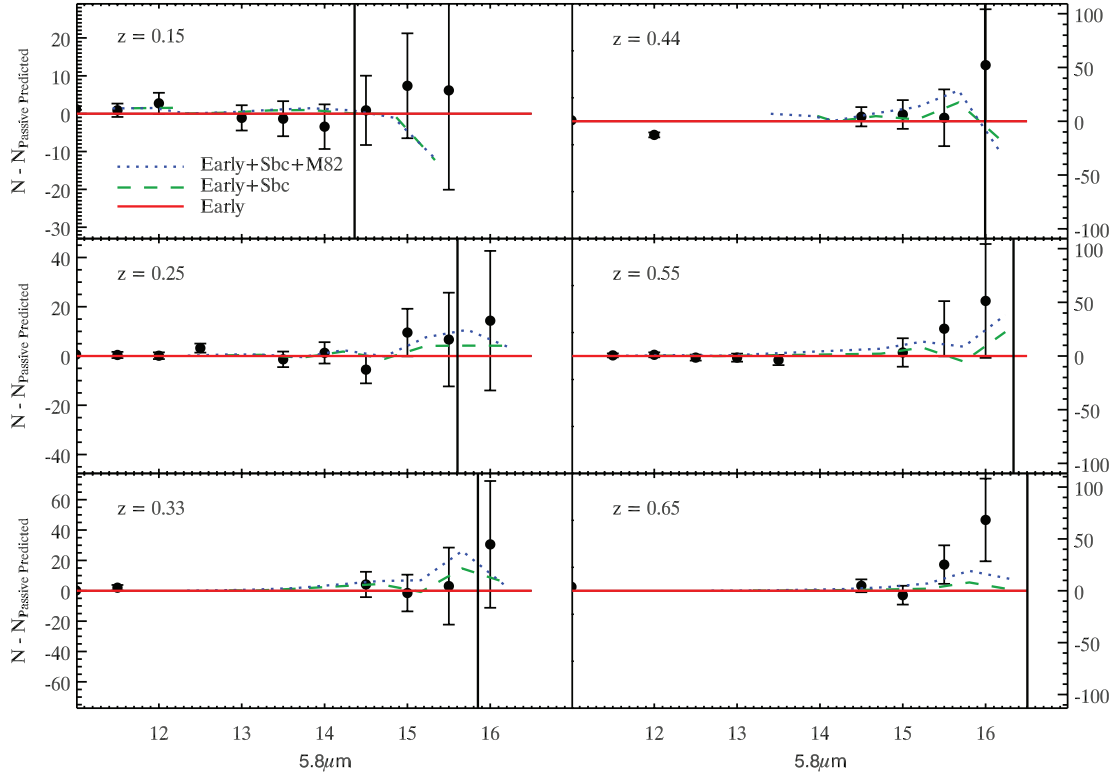


FIG. 18.—Residuals of the cluster $5.8\ \mu\text{m}$ LFs once the predictions from the $3.6\ \mu\text{m}$ LFs and the passive evolution model have been subtracted. The solid red line shows the passive evolution model, the dashed green line shows the regular+quiescent model, and the dotted blue line shows the starburst+regular+quiescent model. The solid vertical line represents the location of M^* from the $3.6\ \mu\text{m}$ LFs assuming the $3.6\ \mu\text{m} - 5.8\ \mu\text{m}$ color of the passive evolution model.

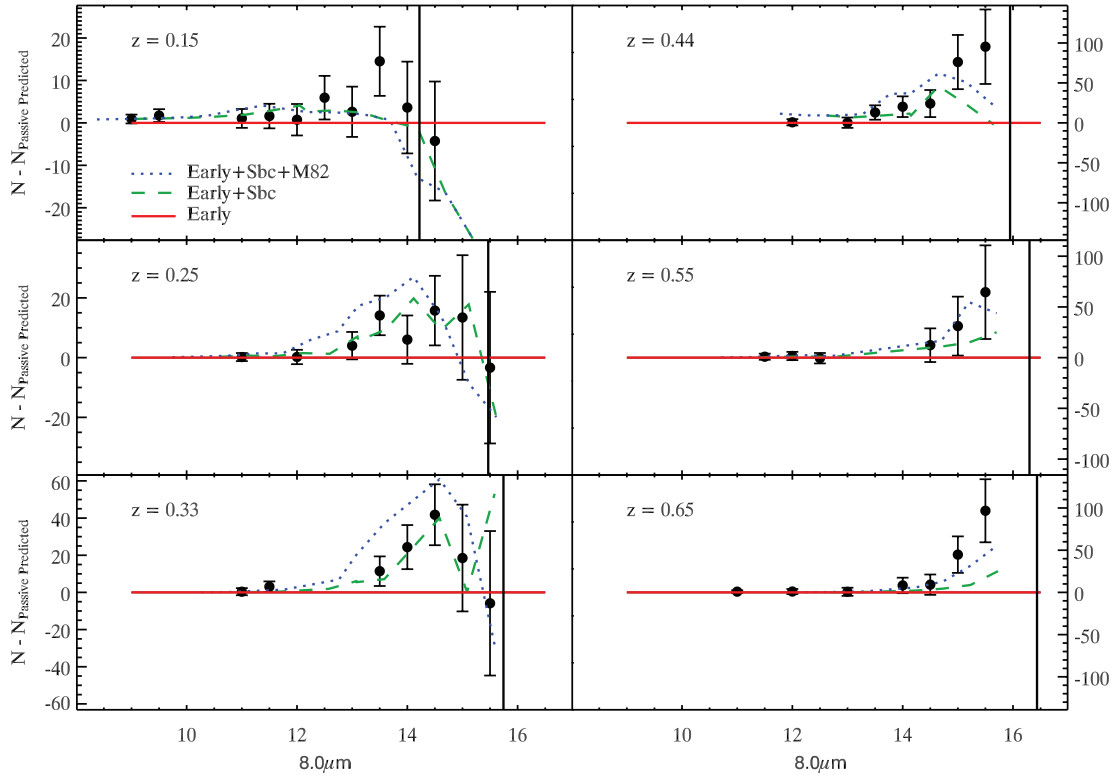


FIG. 19.—Same as Fig. 18, but for the $8.0\ \mu\text{m}$ LFs.

dusty starbursts in the cluster population could be interpreted as the result of an increase in the universal SSFR of galaxies with redshift and the constant accretion of these galaxies into clusters and is not necessarily because starbursts are triggered by the cluster environment. Furthermore, these galaxies might only be considered “starbursts” relative to the mean SSFR locally, whereas at higher redshift their higher SSFR is simply typical of galaxies at that redshift. We compare the cluster 5.8 and 8.0 μm LFs to the field LFs in § 6.2 and discuss this further in that section.

It is interesting that the cluster star-forming population transitions from being best described by regular star-forming galaxies to regular and dusty starburst galaxies around a redshift of $z \sim 0.4$. This is notable because of the discrepant abundances of k+a and a+k poststarburst galaxies found in clusters by the MORPHS (Dressler et al. 1999) and CNOC1 (Balogh et al. 1999) projects. Dressler et al. (1999) found that approximately 18% of cluster galaxy spectra could be classified as k+a galaxies based on the equivalent width of the H δ line, whereas Balogh et al. (1999) found that only 2% of the cluster population could be classified this way. These results obviously lead to very different interpretations of the role of starbursts in the evolution of cluster galaxies. In particular, Dressler et al. (1999) found that the number of k+a galaxies was an order of magnitude higher in clusters than the coeval field, suggesting a cluster-related process to the creation of these galaxies, while Balogh et al. (1999) found roughly equal numbers, suggesting no environmental role.

Although both Dressler et al. (2004) and Balogh et al. (1999) have pointed out that the different methods of data analysis may be partly responsible for such discrepant results, this study suggests that the slightly different redshift range of the MORPHS and CNOC1 sample may also play some role. Excluding the two highest redshift clusters in the CNOC1 sample (MS 0451–03 and MS 0016+16, both at $z \sim 0.55$), the mean redshift of the other 14/16 (88%) clusters in the sample is $z = 0.28$. By contrast, the mean redshift of the MORPHS sample is $z = 0.46$. Our 8.0 μm cluster LFs seem to indicate that $z \sim 0.4$ represents a transition redshift above which the dominant mode of star formation in clusters is better described as starburst, as opposed to regular. Given that once star formation ceases, the typical lifetime of the A star component of a starburst galaxy’s spectrum is ~ 1.5 Gyr, and that the look-back time between $z = 0.46$ and 0.28 is also 1.5 Gyr, it is possible that both dusty starbursts and k+a galaxies that are in clusters at $z = 0.46$ may have evolved to quiescent “k”-type galaxies by $z \sim 0.28$, provided that the dusty star formation is immediately truncated. This would be consistent with the change in the 8.0 μm LFs around this redshift and may explain why the MORPHS and CNOC1 samples show different abundances of poststarburst galaxies. Furthermore, 1.5 Gyr prior to $z = 0.46$ is $z \sim 0.65$. Our $z = 0.65$ cluster LF has the largest abundance of dusty starburst galaxies, and if a significant fraction of these had their star formation truncated, these would be logical progenitors to the large population of k+a galaxies seen at $z = 0.46$ by Dressler et al. (1999).

Our results, which show an increase in the strength of the dominant mode of star formation in cluster galaxies (from weak to normal to starburst), as well as an overall increase in the abundance of dusty star-forming galaxies, are also consistent with MIR observations of other clusters at these redshift ranges. In particular, Coia et al. (2005), Geach et al. (2006), Marcellac et al. (2007), and Bai et al. (2007) have all shown that clusters at higher redshifts have significantly more MIR sources than clusters at lower redshift and that these sources are typically brighter than the sources in lower redshift clusters. Taken at face value, our results and their results show the equivalent of a Butcher-Oemler effect

in the MIR where both the fraction and SSFR of star-forming galaxies are increasing with increasing redshift. Whether this increase is caused by the increase in the universal SFR with redshift and the constant infall of such galaxies into the cluster environment or by the triggering of starbursts by the high-redshift cluster environment is still uncertain. We investigate this point further in § 6.2 by comparing the cluster and field IRAC LFs.

6.2. Is the Cluster Population Different from the Field Population?

The most obvious way to understand if the cluster environment is responsible for triggering starburst events is to directly compare the field and cluster 5.8 or 8.0 μm LFs and look for an excess of galaxies in the cluster LFs. For this comparison we use the field LFs measured by Babbedge et al. (2006). Their LFs are determined using photometric redshifts of $\sim 100,000$ galaxies from a 6.5 deg² patch of the SWIRE survey. The field LFs are measured in five redshift bins, and we compare the cluster LFs to the three bins that overlap the redshift range of the clusters ($0.0 < z < 0.25$, $0.25 < z < 0.50$, and $0.5 < z < 1.0$). The corresponding cluster LFs used for comparison are the $z = 0.15$, 0.33, and 0.65 LFs, respectively.

The Babbedge et al. (2006) field LFs are determined using total luminosities, not apparent magnitudes like for the cluster LFs. Converting the units of the cluster LFs to total luminosities requires distance moduli and full k -corrections. In § 5.2.4 we showed that the cluster LFs can be well described using three basic populations of galaxies: quiescent, regular star-forming, and dusty starburst. We use the models of these three spectral types for the k -corrections. The k -corrections for the quiescent galaxies are taken from the single-burst model, and the k -corrections for the regular and dusty starburst galaxies are taken from the J. Huang et al. (2008, in preparation) Sbc and M82 models, respectively. Each LF is statistically k -corrected using the relative proportions of the galaxies that best described the LFs in § 5.2.4. The apparent LF for each redshift is divided into the three components by the fraction of galaxies of that type and is individually k -corrected and shifted by the distance modulus. These LFs are then summed to provide the total cluster LF in terms of absolute luminosities in units of $\nu L_\nu/L_\odot$.

The cluster LFs are normalized by the number of galaxies per virial volume, whereas the field LFs are normalized by their actual number density per Mpc³. The cluster normalization can be put in the same units as the field LFs by dividing by the virial volume; however, this does not provide a fair comparison because clusters have much higher volume densities of galaxies than the field.

The most useful way to compare the cluster and field LFs is on a per unit stellar mass basis. We do not have stellar mass functions for either the field or cluster; however, we can again assume that the 3.6 μm luminosity is roughly a proxy for stellar mass and renormalize the LFs to a common normalization so that they reproduce the same ϕ^* in the Schechter function fits. The renormalized 3.6, 4.5, 5.8, and 8.0 μm cluster LFs are plotted in Figures 20, 21, 22, and 23, respectively, as the filled red circles. The field LFs are overplotted as blue squares.

Figures 20 and 21 show that the overall shapes of the cluster and field 3.6 and 4.5 μm LFs are similar at all redshifts. There is a slight, although not statistically significant, excess in the number of the brightest galaxies in the cluster LFs; however, these are likely to be giant elliptical galaxies that are common in clusters and typically do not follow the distribution of the Schechter function. Other than the giant ellipticals, the shapes of the 3.6 and 4.5 μm cluster and field LFs are similar, which shows that the

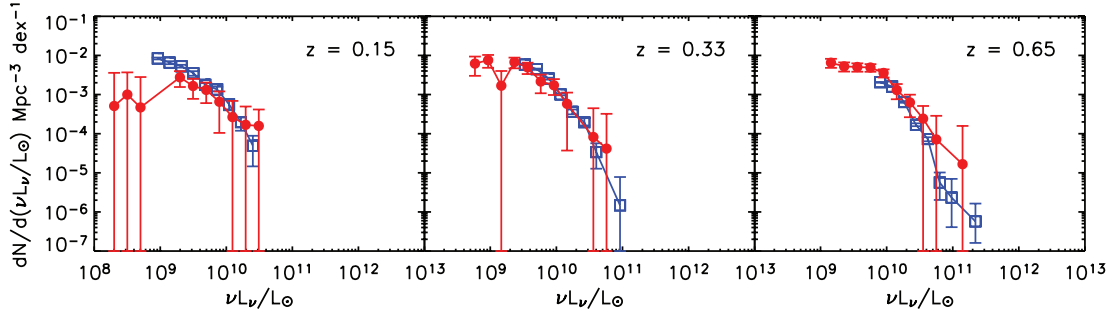


FIG. 20.—Comparison between the cluster and field $3.6\ \mu\text{m}$ LFs at different redshifts. The field LFs are plotted as open blue squares, and the cluster LFs are plotted as filled red circles. The cluster LFs are renormalized so that the values of ϕ^* from the Schechter function fits (§ 5.1) match the ϕ^* values from the Schechter function fits in Babbedge et al. (2006).

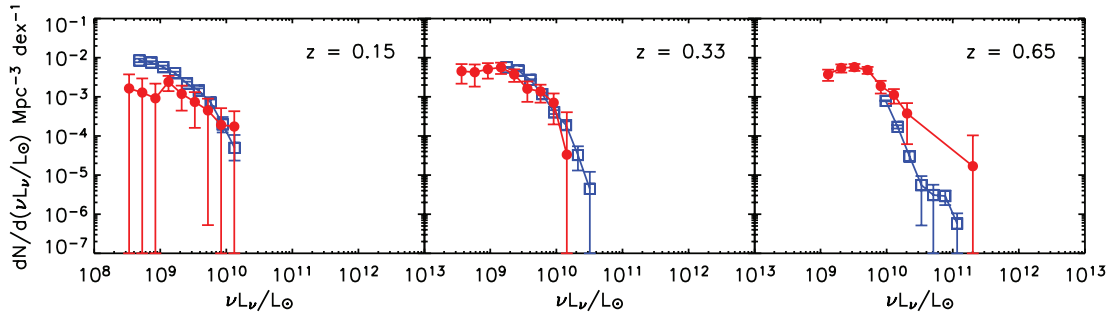


FIG. 21.—Same as Fig. 19, but for the $4.5\ \mu\text{m}$ LFs.

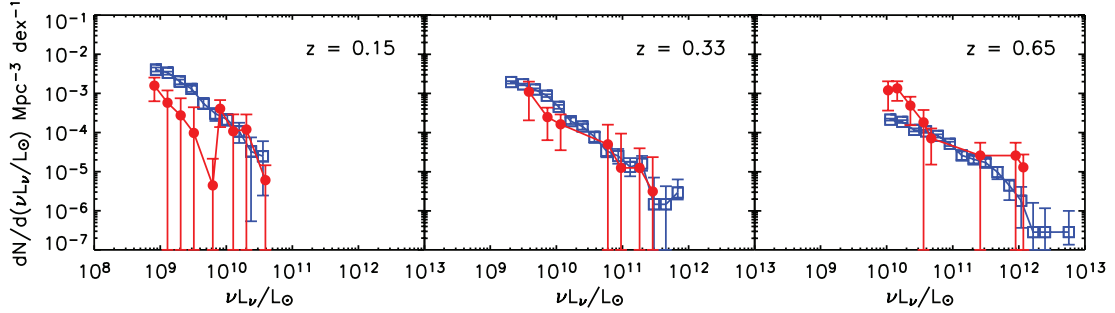


FIG. 22.—Same as Fig. 19, but for the $5.8\ \mu\text{m}$ LFs.

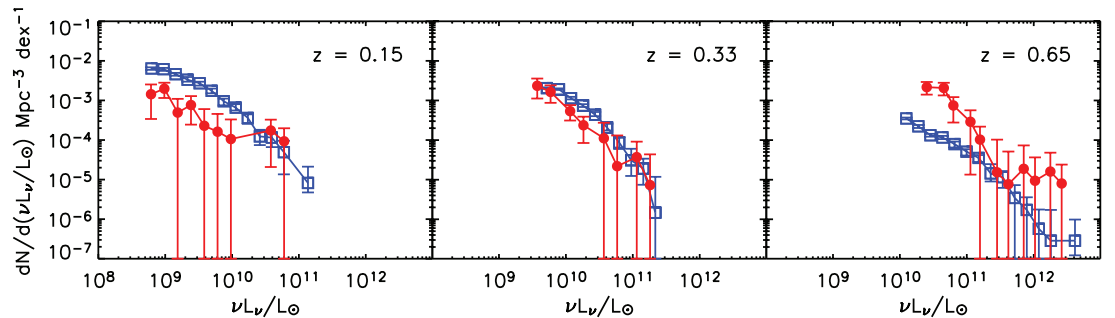


FIG. 23.—Same as Fig. 19, but for the $8.0\ \mu\text{m}$ LFs.

distribution of galaxies as a function of stellar mass is nearly identical in these environments. This result is consistent with *K*-band studies, which have shown only small differences in M^* (<0.2 mag) between these environments (e.g., Balogh et al. 2001; Lin et al. 2004; Rines et al. 2004; Muzzin et al. 2007a).

Conversely, there are significant differences in the 5.8 and 8.0 μm LF of the cluster and field. Both the 5.8 and 8.0 μm LF follow a sequence where the cluster LF is more abundant in MIR galaxies at $z = 0.65$, particularly moderate-luminosity galaxies, and thereafter the abundance of MIR galaxies in clusters declines relative to the field with decreasing redshift. At $z = 0.33$, the cluster is slightly deficient in both 5.8 and 8.0 μm galaxies relative to the field, reduced by a factor of ~ 2 for galaxies with $\nu L_\nu = 5 \times 10^9 - 5 \times 10^{10} L_\odot$. At $z = 0.15$, the cluster LF is significantly depleted compared to the field, reduced by a factor of ~ 5 for galaxies with $\nu L_\nu = 5 \times 10^8 - 5 \times 10^{10} L_\odot$.

This trend indicates not only that the environment of dusty star-forming galaxies affects their evolution, but also that the environmental effects seem to evolve with redshift. At $z = 0.15$ dusty star-forming galaxies are more frequently found in the lower density field environment, whereas at $z = 0.65$ they are found more frequently in the higher density cluster environment.

Our results are similar to those from recent studies by Elbaz et al. (2007) and Cooper et al. (2008) that have shown that the mean SFR of field galaxies in higher density environments increases faster than those in low-density environments with increasing redshift. This differential increase leads to a remarkable reversal in the slope of the $\langle \text{SFR} \rangle$ of galaxies as a function of density at $z \sim 1$ as compared to $z \sim 0$. Field galaxies in high-density environments at $z \sim 1$ actually have higher $\langle \text{SFR} \rangle$ than those in low-density environments. Although those studies compare $\langle \text{SFR} \rangle$ of galaxies at a range of densities within the field and do not use clusters per se, our comparison between the 8 μm LF of the cluster and field environments seems to at least qualitatively suggest a similar trend.

It is not entirely obvious why starbursts should prefer the cluster environment over the field environment at high ($z > 0.5$) redshift and then reject it at lower redshift ($z < 0.5$). We suggest that starbursts could preferentially be triggered during the initial formation and collapse of the cluster and be quenched thereafter by the high-density environment. If this interpretation is correct, it is likely that the parameter most responsible for the change in star formation properties relative to the field is the degree of virialization of the clusters.

Clusters that are unrelaxed, or in the process of collapsing, have two properties that would permit increased numbers of dusty starbursts. First, before virialization, the cluster gas has not yet been shock heated to its maximum temperature. This hot intra-cluster gas has long been considered the primary cause for the quenching of star formation in cluster galaxies because it prevents the cooling of gas in the outer halo of a galaxy, thereby “strangling” star formation. Depending on the density/temperature threshold required for quenching, it is possible that starbursts that would normally be quenched in virialized clusters at lower redshifts may survive longer in unvirialized clusters at high redshift. Secondly, the velocity dispersions in unrelaxed systems are lower and therefore mergers and harassments should be more common at higher redshift (e.g., Tran et al. 2005a). It is plausible that this more dynamically “active” environment preferentially triggers star formation. The combination of more triggered dusty starbursts through harassment and mergers and a weaker quenching process may be the reason for more dusty starbursts in clusters relative to the field at higher redshift. Once a cluster becomes virialized, the interactions between galaxies should become less frequent and the quenching of star formation

by the hot cluster gas will be more efficient. In such a scenario the relative abundances of dusty starbursts in clusters should decrease relative to the field.

If our interpretation is correct, we might expect different results from the 8.0 μm LF of X-ray-selected samples of clusters (i.e., those that require a hot virialized cluster gas component) compared to red-sequence-selected samples, which, assuming that the early-type population is formed prior to cluster collapse, do not require that clusters are fully virialized.

6.3. Are the Color Models Correct?

The main conclusions from the cluster LF presented in this paper depend on interpreting color models that have been primarily calibrated or determined using nearby galaxies. If these models are not applicable at higher redshift, then this could cause incorrect conclusions to be drawn from the LF. Using the spectroscopic redshifts, we can examine the colors of confirmed cluster galaxies as a function of redshift to check if the models are reasonable.

There are 55 spectroscopic redshifts available for cluster galaxies (see §§ 2.4 and 2.5). Using the spectra, we can classify these galaxies into two basic types, star-forming and non-star-forming. For the Hectospec, SDSS, and WYIN spectroscopy the best-fitting cross-correlation template is used for the classification. For the remaining galaxies the classification is made by examining by eye the spectra for any evidence of the [O II], [O III], or H α emission lines. Galaxies with any of these emission lines are classified as star-forming, and those without are classified as non-star-forming. Although this is a crude approach to classifying galaxies, we are only interested in a rough classification, and taking a more quantitative approach, such as measuring EWs, is unnecessary. Furthermore, in all cases the cluster galaxies had spectra that were typical of either normal star-forming (several emission lines including [O II] and H α) or quiescent galaxies (strong H and K lines and a 4000 Å break), and classification was straightforward. There were no hybrid objects associated with clusters except two AGNs from the Hectospec data.

In Figure 24 we plot several of the colors of these galaxies as a function of redshift. Star-forming galaxies are plotted as purple triangles, and non-star-forming galaxies are plotted as red circles. The Bruzual & Charlot single-burst model is overplotted as the solid line, and the J. Huang et al. (2008, in preparation) Sbc and M82 models are overplotted as the dotted and dot-dashed lines, respectively. In general, the non-star-forming galaxies follow the single-burst model well at all redshifts. There are a handful of non-star-forming galaxies that appear to have some excess 8.0 μm emission, and this may be from either low-level star formation or a low-luminosity AGN.

There are fewer star-forming than non-star-forming galaxies in the sample; however, their colors follow the Sbc and M82 models quite well. At 8.0 μm , where the colors of the Sbc and M82 models are most different from the single-burst model, it is clear that galaxies with emission lines have colors similar to those models, whereas those without tend to follow the single-burst model. Half of the star-forming galaxies in Figure 24 (8/16) come from our spectroscopy of FLS J172449+5921.3 (cluster 10, $z = 0.252$). These galaxies were selected for spectroscopy because they were detected at 24 μm . Interestingly, most of these galaxies (7/8) have a 3.6 $\mu\text{m} - 8.0 \mu\text{m}$ color similar to the Sbc model, yet they show a wide range in $R - 3.6 \mu\text{m}$ color. A few have an $R - 3.6 \mu\text{m}$ color bluer than the red sequence, typical of Sbc galaxies, whereas others have an $R - 3.6 \mu\text{m}$ color redder than the red sequence. This illustrates that there are both “red” and “blue” dusty star-forming galaxies in clusters and that our

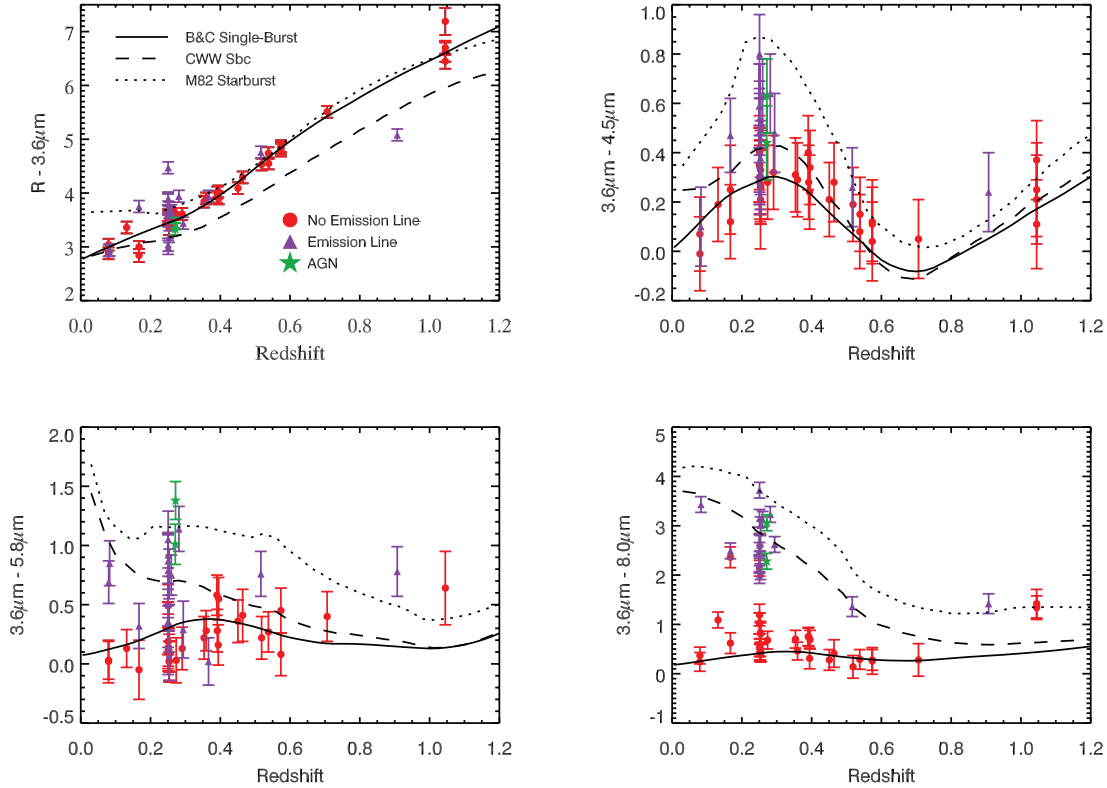


FIG. 24.—Plot of optical-IRAC or IRAC-IRAC colors of galaxies as a function of redshift. The red, purple, and green symbols are spectroscopic cluster members classified as non-star-forming, star-forming, and AGNs, respectively. The solid, dotted, and dashed lines are the model colors from the passive evolution model, the Sbc model, and the M82 model, respectively.

approach of modeling the 5.8 and 8.0 μm LFs with populations of both is reasonable. Furthermore, the fact that these are some of the brightest MIR sources in the cluster field and that most have colors similar to the Sbc model, rather than the M82 model, is consistent with our conclusion that the 8.0 μm LF at this redshift is best modeled using the quiescent+regular model, with no need for a luminous dusty starburst component. We defer a more detailed discussion of the spectroscopy, including quantitative measurements of star formation from line widths, to a future paper (A. Muzzin et al. 2008, in preparation).

Overall, Figure 24 demonstrates that the galaxy templates used to model the cluster LFs agree well with the colors of spectroscopically confirmed cluster galaxies and that they are reasonable descriptions of star-forming and non-star-forming galaxies between $0 < z < 1$.

6.4. Systematic Uncertainties

The data presented in this paper support a self-consistent model of the evolution of stellar mass assembly and dusty star formation in clusters; however, there are several details of this analysis that have not been discussed and could potentially result in inappropriate conclusions being drawn from the data. Although it is difficult to quantify what effect, if any, these details will have on the interpretation of the data, we believe that it is important to at least note these issues here.

One worthwhile concern is the sample of clusters used in the analysis. Although this sample is much larger than the mere handful of clusters that have been studied in the MIR thus far, it is still of modest size and subject to cosmic variance. In particular, given that the clusters come from only 3.8 deg^2 , it is unclear whether the higher redshift clusters in the sample are truly the progenitors of the lower redshift clusters. Unfortunately, a cosmologically significant sample of clusters covering of the order 100 deg^2 or more

is likely needed to avoid biases that might result from cosmic variance in the sample.

Another potential problem is that there are many more low-richness clusters in the sample than high-richness clusters, simply because of the nature of the cluster mass function. Any effects that depend on cluster mass will clearly be missed by combining these samples. This could be important because processes that could quench star formation (e.g., ram pressure stripping, gas strangulation) or incite starbursts (tidal effects, harassment) will likely depend on cluster mass. Using a much larger sample that can be separated by both mass and redshift would be invaluable for studying this issue further.

Perhaps the most important concern is that there is a degeneracy between the intensity of star formation in clusters and the fraction of star-forming galaxies. We showed in § 6.3 that the color models used for the cluster galaxies reproduce the colors of cluster galaxies with spectroscopic redshifts very well; however, even though these colors are correct, the models of the 5.8 and 8.0 μm LFs still depend on the assumed f_b as a function of magnitude and redshift for the clusters. If the f_b values are overestimated and need to be reduced, then a larger fraction of dusty starburst galaxies than we have assumed will be required to correctly model the cluster 5.8 and 8.0 μm LFs. Likewise, if the f_b is underestimated, fewer dusty starbursts will be required. The assumed f_b are consistent with most previous studies; however, optimally, if more data were available, the f_b should be calculated from the clusters themselves and this would avoid this degeneracy.

Lastly, it is worth mentioning that much of the excess seen in the 8.0 μm LFs is near the limiting magnitude of the survey. Problems with the background estimation could artificially inflate these values. It is unlikely that this is the case because if the excess of galaxies near the faint limit of the survey were due to

an undersubtraction of the background, it should also be seen in the lower redshift LFs, which it is not. Furthermore, undersubtraction of the background should be even more prevalent in the lower redshift LFs because clusters have much larger angular sizes and therefore more total area from which to undersubtract the background. It is unlikely that this is a problem; however, deeper data would be useful in ensuring that there are no errors due to completeness near the survey limit.

7. CONCLUSIONS

We have presented a catalog of 99 candidate clusters and groups at $0.1 < z_{\text{phot}} < 1.3$ discovered in the *Spitzer* First Look Survey using the cluster red-sequence technique. Using spectroscopic redshifts from FLS follow-up campaigns and our own spectroscopic follow-up of clusters, we have shown that the $R - 3.6 \mu\text{m}$ color of the cluster red sequence is an accurate photometric redshift estimator at the $\Delta z = 0.04$ level at $z < 1.0$. Furthermore, we demonstrated that the properties of the FLS cluster catalog are similar to previous cluster surveys such as the RCS-1. Using this cluster sample, we studied the evolution of the cluster 3.6, 4.5, 5.8, and $8.0 \mu\text{m}$ LFs. The main results from these LFs can be summarized as follows:

1. In agreement with previous work, the evolution of the 3.6 and $4.5 \mu\text{m}$ LFs between $0.1 < z < 1.0$ is consistent with a passively evolving population of galaxies formed in a single burst at $z > 1.5$. Given that the 3.6 and $4.5 \mu\text{m}$ bandpasses are reasonable proxies for stellar mass, this suggests that the majority of stellar mass in clusters is already assembled into massive galaxies by $z \sim 1$.

2. The MIR color cuts used to select AGNs by Lacy et al. (2004) and Stern et al. (2005) suggest that the fraction of cluster galaxies that host MIR-bright AGNs at $z < 0.7$ is low. We estimate that the AGN fraction of cluster galaxies detected at $3.6 \mu\text{m}$ is $1^{+1}_{-1}\%$. AGNs are a larger, but still modest, component of the 5.8 and $8.0 \mu\text{m}$ cluster population, approximately $3^{+3}_{-3}\%$ of these galaxies.

3. The cluster 5.8 and $8.0 \mu\text{m}$ LFs do not look similar to the 3.6 and $4.5 \mu\text{m}$ LFs, and this is due to the presence of the cluster star-forming galaxies. Star-forming galaxies are much brighter in these bandpasses than early-type galaxies, and their varying fractions with redshift cause deviations from the shape of the 3.6 and $4.5 \mu\text{m}$ LFs. The 5.8 and $8.0 \mu\text{m}$ LFs are well described using different fractions of three basic types of galaxies, quiescent, regular star-forming, and dusty starburst, by assuming that the fractions of the latter two are proportional to the cluster f_b .

4. The $8.0 \mu\text{m}$ cluster LFs suggest that both the frequency and SSFR of star-forming cluster galaxies are increasing with increasing redshift. In particular, it appears that when compared to star-forming galaxies in the local universe, the intensity of star formation in clusters evolves from “weak” to “regular” to “starburst” with increasing redshift. Qualitatively, this evolution mimics the evolution in the universal star formation density with redshift, suggesting that this evolution is at least in part caused by the accretion of star-forming galaxies into the cluster environment.

5. Comparing the 3.6 and $4.5 \mu\text{m}$ cluster and field LFs with similar normalization shows that the LFs in these environments are similar, with evidence for a small excess in the brightest galaxies in clusters, likely caused by the cluster giant ellipticals. In agreement with previous K -band studies, this suggests that the distribution of galaxies as a function of stellar mass in both environments is roughly equivalent.

6. There is a significant differential evolution in the cluster and field 5.8 and $8.0 \mu\text{m}$ LFs with redshift. At $z = 0.65$ the cluster is more abundant in $8.0 \mu\text{m}$ galaxies than the field; however,

thereafter the relative number of 5.8 and $8.0 \mu\text{m}$ galaxies declines in clusters with decreasing redshift, and by $z = 0.15$ the cluster is underdense in these sources by roughly a factor of 5. This differential evolution could be explained if starbursts are preferentially triggered during the early formation stages of the cluster but then preferentially quenched thereafter by the high-density environment.

A well-sampled spectroscopic study of several high-redshift clusters with MIR data would be extremely valuable for verifying our interpretation of the IRAC cluster LFs because it is always difficult to draw incontrovertible conclusions from LFs alone. Still, the cluster LFs do show a strong increase in the number of 5.8 and $8.0 \mu\text{m}$ sources in clusters with increasing redshift, which must almost certainly be attributed to increased amounts of dusty star formation in higher redshift clusters.

One of the strengths of this analysis is that it is based on a relatively large sample of galaxy clusters. It has become clear from the handful of clusters studied thus far by *ISO* and *Spitzer* that the MIR properties of cluster galaxies can be quite different from cluster to cluster. They may depend on dynamical state, mass, f_b , or other parameters (e.g., Coia et al. 2005; Geach et al. 2006). The advantage of using many clusters is that it provides a metric of how the “average” cluster is evolving as a function of redshift. Detailed studies of individual clusters with significant ancillary data will pave the way to a better understanding of the physics behind the evolution of dusty star formation in cluster galaxies; however, large statistical studies such as this one will indicate whether the clusters studied in future work are representative of the cluster population as a whole or are potentially rare, biased clusters with unusual properties caused by an ongoing merger or some other event.

It is worth noting that although the quality of the LFs provided by the 99 clusters in the FLS is good, these LFs would still benefit from a larger statistical sample. In particular, a larger sample would allow for the separation of clusters by other properties, such as mass or morphology, and would allow us to understand if these properties play a role in shaping the MIR cluster galaxy population. We are currently working on a survey to detect clusters in the much larger SWIRE survey: the *Spitzer* Adaptation of the Red sequence Cluster Survey (SpARCS). This project has 13 times more area than the FLS and is a factor of 2 deeper in integration time in the IRAC bands. The analysis of that sample should provide a significant improvement in the quality of the cluster LFs.

We thank the anonymous referee, whose comments improved this manuscript significantly. We would like to thank David Gilbank, Thomas Babbedge, Roberto De Propriis, and Stefano Andreon for graciously making their data available to us. We thank David Gilbank for useful conversations that helped improve the clarity of this analysis. We also thank Dario Fadda for recomputing the FLS R -band photometry using different apertures. A. M. acknowledges support from the *Spitzer* Visiting Graduate Student Program during which much of this work was completed. A. M. also acknowledges support from the National Sciences and Engineering Research Council (NSERC) in the form of PGS-A and PGSD2 fellowships. The work of H. K. C. Y. is supported by grants from the Canada Research Chair Program, NSERC, and the University of Toronto. This work is based in part on observations made with the *Spitzer Space Telescope*, which is operated by the Jet Propulsion Laboratory, California Institute of Technology under a contract with NASA.

REFERENCES

- Abell, G. O. 1958, *ApJS*, 3, 211
- Abraham, R. G., et al. 1996, *ApJ*, 471, 694
- Adelman-McCarthy, J. K., et al. 2007, *ApJS*, 172, 634
- Andreoni, S. 2006, *A&A*, 448, 447
- Andreoni, S., Lobo, C., & Iovino, A. 2004, *MNRAS*, 349, 889
- Babbedge, T. S. R., et al. 2006, *MNRAS*, 370, 1159
- Bahcall, N. A., et al. 2003, *ApJS*, 148, 243
- Bai, L., et al. 2007, *ApJ*, 664, 181
- Balogh, M., Morris, S. L., Yee, H. K. C., Carlberg, R. G., & Ellingson, E. 1999, *ApJ*, 527, 54
- Balogh, M. L., Christlein, D., Zabludoff, A. I., & Zaritsky, D. 2001, *ApJ*, 557, 117
- Balogh, M. L., et al. 2007, *MNRAS*, 374, 1169
- Barkhouse, W. A., et al. 2006, *ApJ*, 645, 955
- Bekki, K., & Couch, W. J. 2003, *ApJ*, 596, L13
- Bell, E., & de Jong, R. S. 2001, *ApJ*, 550, 212
- Bell, E., McIntosh, D. H., Katz, N., & Weinberg, M. D. 2003, *ApJS*, 149, 289
- Bertin, E., & Arnouts, S. 1996, *A&AS*, 117, 393
- Biviano, A., et al. 2004, *A&A*, 425, 33
- Blakeslee, J. P., et al. 2003, *ApJ*, 596, L143
- Blindert, K., Yee, H. K. C., Gladders, M. D., & Ellingson, E. 2004, in *IAU Colloq. 195, Outskirts of Galaxy Clusters: Intense Life in the Suburbs*, ed. A. Diaferio (Cambridge: Cambridge Univ. Press), 215
- Bower, R. G., Lucey, J. R., & Ellis, R. S. 1992, *MNRAS*, 254, 601
- Brinchmann, J. 1999, Ph.D. thesis, Cambridge Univ.
- Brodwin, M., et al. 2006, *ApJ*, 651, 791
- Bruzual, G., & Charlot, S. 2003, *MNRAS*, 344, 1000
- Butcher, H., & Oemler, A. J. 1984, *ApJ*, 285, 426
- Calzetti, D., et al. 2005, *ApJ*, 633, 871
- Calzetti, D., et al. 2007, *ApJ*, 666, 870
- Cardamone, C. N., et al. 2008, *ApJ*, 680, 130
- Choi, P., et al. 2006, *ApJ*, 637, 227
- Christlein, D., & Zabludoff, A. I. 2005, *ApJ*, 621, 201
- Coia, D., et al. 2005, *A&A*, 431, 433
- Coleman, G. D., Wu, C.-C., & Weedman, D. W. 1980, *ApJS*, 43, 393
- Cooper, M., et al. 2008, *MNRAS*, 383, 1058
- Cortese, L., et al. 2007, *MNRAS*, 376, 157
- Dale, D. A., et al. 2005, *ApJ*, 633, 857
- De Propriis, R., Stanford, S. A., Eisenhardt, P. R., Dickinson, M., & Elston, R. 1999, *AJ*, 118, 719
- De Propriis, R., Stanford, S. A., Eisenhardt, P. R., Holder, B. P., & Rosati, P. 2007, *AJ*, 133, 2209
- Dressler, A., Oemler, A., Poggianti, B., Smail, I., Trager, S., Schechtman, S., Couch, W., & Ellis, R. S. 2004, *ApJ*, 617, 867
- Dressler, A., Rigby, J., Oemler, A., Fritz, J., Poggianti, B., Rieke, G., & Bai, L. 2008, *ApJ*, submitted (arXiv:0806.2343)
- Dressler, A., Smail, I., Poggianti, B. M., Butcher, H., Couch, W. J., Ellis, R. S., & Oemler, A. 1999, *ApJS*, 122, 51
- Dressler, A., Thompson, I. B., & Schechtman, S. A. 1985, *ApJ*, 288, 481
- Dressler, A., et al. 1997, *ApJ*, 490, 577
- Duc, P.-A., et al. 2002, *A&A*, 382, 60
- Eastman, J., Martini, P., Sivakoff, G., Kelson, D. D., Mulchaey, J. S., & Tran, K.-V. 2007, *ApJ*, 664, L9
- Eisenhardt, P., et al. 2004, *ApJS*, 154, 48
- . 2008, *ApJ*, 684, 905
- Elbaz, D., et al. 2007, *A&A*, 468, 33
- Ellingson, E., Lin, H., Yee, H. K. C., & Carlberg, R. G. 2001, *ApJ*, 547, 609
- Ellis, R. S., Smail, I., Dressler, A., Couch, W. J., Oemler, A., Butcher, H., & Sharples, R. M. 1997, *ApJ*, 483, 582
- Faber, S., et al. 2003, *Proc. SPIE*, 4841, 1657
- Fadda, D., Biviano, A., Marleau, F. R., Storrie-Lombardi, L. J., & Durret, F. 2008, *ApJ*, 672, L9
- Fadda, D., Elbaz, D., Duc, P.-A., Flores, H., Franceschini, A., Cesarsky, C. J., & Moorwood, A. F. M. 2000, *A&A*, 361, 827
- Fadda, D., Jannuzi, B. T., Ford, A., & Storrie-Lombardi, L. J. 2004, *AJ*, 128, 1
- Gallazzi, A., Charlot, S., Brinchmann, J., & White, S. D. M. 2006, *MNRAS*, 370, 1106
- Geach, J. E., et al. 2006, *ApJ*, 649, 661
- Gilbank, D. G., Bower, R. G., Castander, F. J., & Ziegler, B. L. 2004, *MNRAS*, 348, 551
- Gilbank, D. G., Yee, H. K. C., Ellingson, E., Gladders, M. D., Barrientos, L. F., & Blindert, K. 2007, *AJ*, 134, 282
- Gillett, F. C., Forrest, W. J., & Merrill, K. M. 1973, *ApJ*, 183, 87
- Gladders, M. D., Lopez-Cruz, O., Yee, H. K. C., & Kodama, T. 1998, *ApJ*, 501, 571
- Gladders, M. D., & Yee, H. K. C. 2000, *AJ*, 120, 2148 (GY00)
- . 2005, *ApJS*, 157, 1
- Glazebrook, K., et al. 2004, *Nature*, 430, 181
- Haiman, Z., Mohr, J. J., & Holder, G. P. 2001, *ApJ*, 553, 545
- Holden, B. P., Stanford, S. A., Eisenhardt, P., & Dickinson, M. 2004, *AJ*, 127, 2484
- Holden, B. P., et al. 2005, *ApJ*, 620, L83
- Homeier, N. L., et al. 2006, *ApJ*, 647, 256
- Huang, J.-S., et al. 2007, *ApJ*, 664, 840
- Kodama, T., Balogh, M. L., Smail, I., Bower, R. G., & Nakata, F. 2004, *MNRAS*, 354, 1103
- Koester, B. P., et al. 2007, *ApJ*, 660, 239
- Kravtsov, A. V., Berlind, A. A., Wechsler, R. H., Klypin, A. A., Gottlöber, S., Allgood, B., & Primack, J. R. 2004, *ApJ*, 609, 35
- Lacy, M., et al. 2004, *ApJS*, 154, 166
- Lacy, M., et al. 2005, *ApJS*, 161, 41
- Le Floch, E., et al. 2005, *ApJ*, 632, 169
- Lilly, S. J., Le Fèvre, O., Hammer, F., & Crampton, D. 1996, *ApJ*, 460, L1
- Lin, Y.-T., Mohr, J. J., Gonzalez, A. H., & Stanford, S. A. 2006, *ApJ*, 650, L99
- Lin, Y.-T., Mohr, J. J., & Stanford, S. A. 2003, *ApJ*, 591, 749
- . 2004, *ApJ*, 610, 745
- Loh, Y. S., Ellingson, E., Yee, H. K. C., Gladders, M. D., Barrientos, L. F., & Gilbank, D. G. 2008, *ApJ*, 680, 214
- Longair, M. S., & Seldner, M. 1979, *MNRAS*, 189, 433
- Lonsdale, C. J., et al. 2003, *PASP*, 115, 897
- Lopez-Cruz, O., Barkhouse, W. A., & Yee, H. K. C. 2004, *ApJ*, 614, 679
- Magnelli, B., Chary, R. R., Pope, A., Elbaz, D., Morrison, G., & Dickinson, M. 2008, *ApJ*, 681, 258
- Marcillac, D., Rigby, J. R., Rieke, G. H., & Kelly, D. M. 2007, *ApJ*, 654, 825
- Margoniner, V. E., De Carvalho, R. R., Gal, R. R., & Djorgovski, S. G. 2001, *ApJ*, 548, L143
- Marleau, F. R., Fadda, D., Appleton, P. N., Noriega-Crespo, A., Im, M., & Clancy, D. 2007, *ApJ*, 663, 218
- Martini, P., Kelson, D. D., Kim, E., Mulchaey, J. S., & Athey, A. A. 2006, *ApJ*, 644, 116
- Martini, P., Mulchaey, J. S., & Kelson, D. D. 2007, *ApJ*, 664, 761
- Massey, P., & Gronwall, C. 1990, *ApJ*, 358, 344
- McCarthy, P. J., et al. 2004, *ApJ*, 614, L9
- Mei, S., et al. 2006, *ApJ*, 644, 759
- Metevier, A. J., Romer, A. K., & Ulmer, M. P. 2000, *AJ*, 119, 1090
- Monet, D., et al. 1998, *USNO-A2.0 Catalog* (Flagstaff: US Naval Obs.)
- Moran, S. M., Ellis, R. S., Treu, T., Salim, S., Rich, R. M., Smith, G. P., & Kneib, J.-P. 2006, *ApJ*, 641, L97
- Moran, S. M., Ellis, R. S., Treu, T., Smail, I., Dressler, A., Coil, A. L., & Smith, G. P. 2005, *ApJ*, 634, 977
- Moss, C., & Whittle, M. 2000, *MNRAS*, 317, 667
- Muzzin, A., Yee, H. K. C., Hall, P. B., Ellingson, E., & Lin, H. 2007a, *ApJ*, 659, 1106
- Muzzin, A., Yee, H. K. C., Hall, P. B., & Lin, H. 2007b, *ApJ*, 663, 150
- Nelan, J. E., Smith, R. J., Hudson, M. J., Wegner, G. A., Lucey, J. R., Moore, S. A., W., Quinney, S. J., & Suntzeff, N. B. 2005, *ApJ*, 632, 137
- Owen, F. N., Ledlow, M. J., Keel, W. C., & Morrison, G. E. 1999, *AJ*, 118, 633
- Owen, F. N., Ledlow, M. J., Keel, W. C., Wang, Q. D., & Morrison, G. E. 2005, *AJ*, 129, 31
- Papovich, C., et al. 2006, *AJ*, 132, 231
- Pérez-González, P. G., et al. 2005, *ApJ*, 630, 82
- Poggianti, B., et al. 2006, *ApJ*, 642, 188
- Poggianti, B. M., Smail, I., Dressler, A., Couch, W. J., Barger, A. J., Butcher, H., Ellis, R. S., & Oemler, A. 1999, *ApJ*, 518, 576
- Popesso, P., Biviano, A., Romaniello, M., & Böhringer, H. 2007, *A&A*, 461, 411
- Postman, M., et al. 2005, *ApJ*, 623, 721
- Press, W. H., Teukolsky, S. A., Vetterling, W. T., & Flannery, B. P. 1992, *Numerical Recipes in FORTRAN 77*, Vol. 1 (2nd ed.; Cambridge: Cambridge Univ. Press)
- Rakos, K. D., & Schombert, J. M. 1995, *ApJ*, 439, 47
- Rines, K., Geller, M. J., Diaferio, A., Kurtz, M. J., & Jarrett, T. H. 2004, *AJ*, 128, 1078
- Rines, K., Geller, M. J., Kurtz, M. J., & Diaferio, A. 2005, *AJ*, 130, 1482
- Saintonge, A., Tran, K.-V., & Holden, B. P. 2008, *ApJ*, submitted (arXiv:0806.2157)
- Schechter, P. 1976, *ApJ*, 203, 297
- Schimminovich, D., et al. 2005, *ApJ*, 619, L47
- Shioya, Y., Bekki, K., & Couch, W. J. 2004, *ApJ*, 601, 654
- Skrutskie, M. F., et al. 2006, *AJ*, 131, 1163
- Smail, I., Edge, A., Ellis, R. S., & Blandford, R. D. 1998, *MNRAS*, 293, 124
- Smith, G. P., Treu, T., Ellis, R. S., Moran, S. M., & Dressler, A. 2005, *ApJ*, 620, 78
- Stanford, S. A., Eisenhardt, P. R., & Dickinson, 1998, *ApJ*, 492, 461
- Stern, D., et al. 2005, *ApJ*, 631, 163
- Strazzullo, V., et al. 2006, *A&A*, 450, 909
- Toft, S., Mainieri, V., Rosati, P., Lidman, C., Demarco, R., Nonino, M., & Stanford, S. A. 2004, *A&A*, 422, 29

- Tran, K.-V. H., Franx, M., Illingworth, G. D., van Dokkum, P., Kelson, D. D., Blakeslee, J. P., & Postman, M. 2007, *ApJ*, 661, 750
- Tran, K.-V. H., van Dokkum, P., Franx, M., Illingworth, G. D., Kelson, D. D., & Schreiber, N. M. F. 2005a, *ApJ*, 627, L25
- Tran, K.-V. H., van Dokkum, P., Illingworth, G. D., Kelson, D., Gonzalez, A., & Franx, M. 2005b, *ApJ*, 619, 134
- Treu, T., et al. 2003, *ApJ*, 591, 53
- van Dokkum, P. G., Franx, M., Kelson, D. D., & Illingworth, G. 1998, *ApJ*, 504, L17
- van Dokkum, P. G., & Stanford, S. A. 2003, *ApJ*, 585, 78
- Willner, S. P., Soifer, B. T., Russell, R. W., Joyce, R. R., & Gillett, F. C. 1977, *ApJ*, 217, L121
- Wilson, G., Cowie, L. L., Barger, A. J., & Burke, D. J. 2002, *AJ*, 124, 1258
- Wilson, G., et al. 2007, *ApJ*, 660, L59
- Wolf, C., Gray, M. E., & Meisenheimer, K. 2005, *A&A*, 443, 435
- Wu, H., Cao, C., Hao, C.-N., Liu, F.-S., Wang, J.-L., Xia, X.-Y., Deng, Z.-G., & Young, C. K.-S. 2005, *ApJ*, 632, L79
- Yee, H. K. C., & Ellingson, E. 2003, *ApJ*, 585, 215
- Yee, H. K. C., Gladders, M. D., Gilbank, D. G., Majumdar, S., Hoekstra, H., & Ellingson, E. 2007, preprint (astro-ph/0701839)
- Yee, H. K. C., & Lopez-Cruz, O. 1999, *AJ*, 117, 1985
- Zwicky, F., Herzog, E., & Wild, P. 1961, *Catalogue of Galaxies and Clusters of Galaxies* (Pasadena: Caltech)